QCD with dynamical Wilson fermions. II

Rajan Gupta
T-8, MS-B285, Los Alamos National Laboratory, Los Alamos, New Mexico 87545

Clive F. Baillie
Physics Department, University of Colorado, Boulder, Colorado 80309

Ralph G. Brickner
C-Division, Los Alamos National Laboratory, Los Alamos, New Mexico 87545

Gregory W. Kilcup
Physics Department, The Ohio State University, Columbus, Ohio 43210

Apoorva Patel
Supercomputer Education and Research Centre and Centre for Theoretical Studies, Indian Institute of Science, Bangalore 560012, India

Stephen R. Sharpe
Physics Department, University of Washington, Seattle, Washington 98195
(Received 20 June 1991)

We present results for the QCD spectrum and the matrix elements of scalar and axial-vector densities at $\beta=6/g^2=5.4,5.5,5.6$. The lattice update was done using the hybrid Monte Carlo algorithm to include two flavors of dynamical Wilson fermions. We have explored quark masses in the range $m_s \leq m_q \leq 3m_s$. The results for the spectrum are similar to quenched simulations and mass ratios are consistent with phenomenological heavy-quark models. The results for matrix elements of the scalar density show that the contribution of sea quarks is comparable to that of the valence quarks. This has important implications for the pion-nucleon σ term.

I. INTRODUCTION

In this paper we present results of simulations of QCD with two degenerate flavors of Wilson fermions. We have generated lattices using the hybrid Monte Carlo (HMC) algorithm [1] at $\beta=5.4$, 5.5, and 5.6. At each of these values of β we have simulated a number of values of κ as described in Table I. This exploration of parameter space is necessary in order to (a) evaluate the behavior and efficiency of the HMC algorithm as we reduce the quark mass, (b) determine the chiral limit (κ_c) and the lattice scale for each of the three values of β, (c) study the effect of quark loops as a function of the quark mass, and (d) examine the scaling behavior of observables.

The details of our implementation of the HMC algorithm and tests on 8^4 lattices were presented in Ref. [2]. In Secs. II and III we discuss the efficiency of the HMC algorithm on larger lattices (16^4 and $16^3\times32$), at weaker coupling, and at smaller quark masses. Most of the update was done on the Connection Machine 2 (CM2). Our present version of the code runs at a sustained speed of over 5 Gflops. The technical details of the implementation and the tests carried out are discussed in Appendix A.

In this paper we present results for the following analyses: (a) screening in the $q\bar{q}$ potential using Wilson loop expectation values (Sec. IV), (b) hadron spectrum (Secs. V and VI), and (c) the scalar density and axial-vector matrix elements (Sec. VII). A preliminary version of these results has been presented in Ref. [3]. Results for the moments of the pion distribution function are given in Ref. [4]. The calculation of the $I=2$ $\pi\pi$ scattering length and weak matrix elements leading to the parameter B_K arising in $K^0-\bar{K}^0$ mixing is in progress. These first results show that we have reached a stage where calculations including the effects of dynamical fermions can be done on lattices as large as $16^3\times32$ with precision comparable to quenched simulations for $m_q \geq m_s$. The limitations of the present calculation are that the results are obtained for quark masses in the range $m_s < m_q < 3m_s$, and that the weakest coupling used, $\beta=5.6$, is at best just at the beginning of the scaling region.

II. OPTIMIZING HMC ALGORITHM

The parameters used in the update and the statistics for all the runs done so far are presented in Table I. The step size ϵ is selected to give $\sim70\%$ acceptance. We use trajectories of variable length in the molecular-dynamics (MD) evolution of the system: the length is $[i+j\times\mathrm{ran}f(\ )]$ steps. The two integers, $(i;j)$ [listed under the heading $N_{\mathrm{MD}}(i;j)$ in Table I], are selected to

TABLE I. (a) Run parameters for the 16^4 lattices after thermalization. The trajectories are of random length $N_{\rm MD}=i+j\times{\rm ran}f(\ )$. The number of trajectories generated before ($N_{\rm traj}^{\rm old}$) and after ($N_{\rm traj}^{\rm new}$) fixing the bug are given separately along with corresponding acceptance rates. (b) Run parameters for the $16^3\times 32$ lattices after thermalization. The trajectories are of random length $N_{\rm MD}=i+j\times{\rm ran}f(\ )$. Only the Wilson loop data from these runs has been included in the present analysis.

β	κ_d	ϵ	$N_{\rm MD}(i;j)$	$N_{\rm traj}^{\rm old}$	$N_{\rm traj}^{\rm new}$	Accep.
			(a)			
5.4	0.160	0.017	45;20		600	−;60%
5.4	0.161	0.015	50;20		1080	−;61%
5.4	0.162	0.010	70;35	310		74;−%
5.5	0.158	0.011	70;30	320		60;−%
5.5	0.159	0.010	70;40	400		60;−%
5.5	0.160	0.008	100;40	400	135	62;68%
5.6	0.156	0.013	60;30	220	460	84;73%
5.6	0.157	0.009	80;40	440	480	60;78%

β	κ_d	ϵ	$\log_{10}R$	$N_{\rm MD}(i;j)$	$N_{\rm traj}$	Accep.
			(b)			
5.5	0.160	0.007	−15	120;60	300	70%
5.6	0.157	0.0085	−14	100;50	400	69%
5.6	0.1575	0.008	−15	60;30	280	65%

TABLE II. Performance of the inversion algorithm during update on the 16^4 lattices. R is the convergence criterion. MR(1) and MR(2) are the number of iterations required for the two steps in the fourth-order algorithm described in Ref. [2]. Cases where data does not exist have been left blank.

β	κ_d	$\log_{10}R$	MR(1)	MR(2)
5.4	0.160	−12		49
5.4	0.161	−13		68
5.4	0.162	−13	63	81
5.5	0.158	−13		
5.5	0.159	−14	84	110
5.5	0.160	−15	145	185
5.6	0.156	−14	78	100
5.6	0.157	−14	110	150
5.6	0.1575	−12	98	150
5.6	0.1575	−13	114	165
5.6	0.1575	−14	135	185
5.6	0.1575	−15	155	202

make the average trajectory of approximately unit length. It has been argued by Mackenzie [5] that using a trajectory of random length helps decorrelate the system faster when there exist well-defined Fourier modes. For individual molecular-dynamics trajectories, QCD does appear to have low-frequency periodic modes [6]. Whether such modes persist over all phase space with the same period is not established for a highly nonlinear, strongly interacting theory such as QCD. Nevertheless, we use a trajectory of random length to avoid the possibility of getting locked into a periodic orbit.

The HMC algorithm has only one source of systematic error: lack of accuracy in the matrix inversions occurring in the molecular-dynamics evolution and in the calculation of the action. Throughout this paper our convergence parameter is defined by

$$R=\left|\frac{r}{\chi}\right|^2=\left|\frac{M\chi-\phi}{\chi}\right|^2, \tag{2.1}$$

where χ is the "solution" vector, ϕ is the source vector, and M is the operator matrix (the preconditioning factors times the fermion matrix). We monitor the effect of inversion error by calculating the change in the action during a trajectory, ΔS, as a function of R. We pick a value for R for which the error in ΔS is $<1\%$. For example, in a particular instance at $\beta=5.6$ and $\kappa=0.1575$, we find that $\Delta S=0.4893$, 0.4274, 0.4153, 0.4138 for $R=10^{-12},10^{-13},10^{-14},10^{-15}$, respectively, and we pick $R=5\times10^{-15}$ as our criterion for production runs. The values of R used in the runs are given in Table II. The mean number of iterations necessary for convergence in each of the two steps of our preconditioned (fourth order in κ), over-relaxed minimal residue algorithm [2] are also given in Table II. The fluctuation in the number of iterations is $\sim 10\%$ about the value quoted. The number of iterations necessary for convergence is positively correlated with the plaquette; i.e., in the confined phase the number of iterations required is larger when the value of the plaquette is larger.

The HMC algorithm has a number of tunable parameters: $\beta_{\rm MD}$, $\kappa_{\rm MD}$, ϵ, and the trajectory length. In this study we use trajectories of length ~ 1 unit of MD time. We try to choose the step size ϵ to maximize the rate of motion through phase space in CPU time, i.e., maximize $\epsilon\times$ (acceptance). The optimal ϵ is then itself maximized as a function of $\beta_{\rm MD}$ and $\kappa_{\rm MD}$. With our limited statistics it is difficult to use this method. Instead, we recall from past studies that the optimal acceptance is $\approx 70\%$, and that this acceptance occurs if ΔS lies in the range $[-1,1]$. We then adopt this last criterion for our optimization, and carry out detailed tests on a few trajectories.

The method we use is as follows. For a given value of β, κ, and lattice size we pick a thermalized lattice. We study the trajectory starting from this lattice for a fixed random number seed, so that both the pseudofermions and the initial momenta conjugate to the gauge fields are always the same. We fix the length of the trajectory to be approximately 1.5 units, i.e., somewhat longer than the trajectories used in production runs. We calculate the ΔS after each molecular-dynamics step, rather then just at the end of the trajectory. We then make the following runs for a number of starting lattices.

(1) We set $\kappa_{\rm MD}=\kappa$ and $\beta_{\rm MD}=\beta$ and vary ϵ. We see three features in the data: (a) $\Delta S\to 0$ as $\epsilon\to 0$ as must be the case; (b) the fluctuations in ΔS decrease as $\epsilon\to 0$; and (c) the evolution decorrelates more quickly in molecular-dynamics time as ϵ is increased, in the sense that the peaks and valleys do not correspond. In Fig. 1(a) we show an example of the dependence of ΔS on ϵ. Based on

such runs we choose a value of ϵ for which ΔS fluctuates between $[-1,1]$ over the length of the trajectory.

(2) Having fixed ϵ, we make runs with different values of κ_{MD} keeping $\beta_{MD}=\beta$. In Figs. 1(b) and 1(c) we show the results of picking $\kappa_{MD}<\kappa$ and $\kappa_{MD}>\kappa$, respectively. In most of our test runs we find that the fluctuations in ΔS are larger than in the reference run with $\kappa_{MD}=\kappa$.

(3) We also use different values of β_{MD} keeping $\kappa_{MD}=\kappa$. Again, as shown in Figs. 1(d) and 1(e), the situation deteriorates for both cases $\beta_{MD}<\beta$ and $\beta_{MD}>\beta$.

Based on our tests, we conclude that nearly optimal tuning for 16^4 lattices is achieved simply by setting

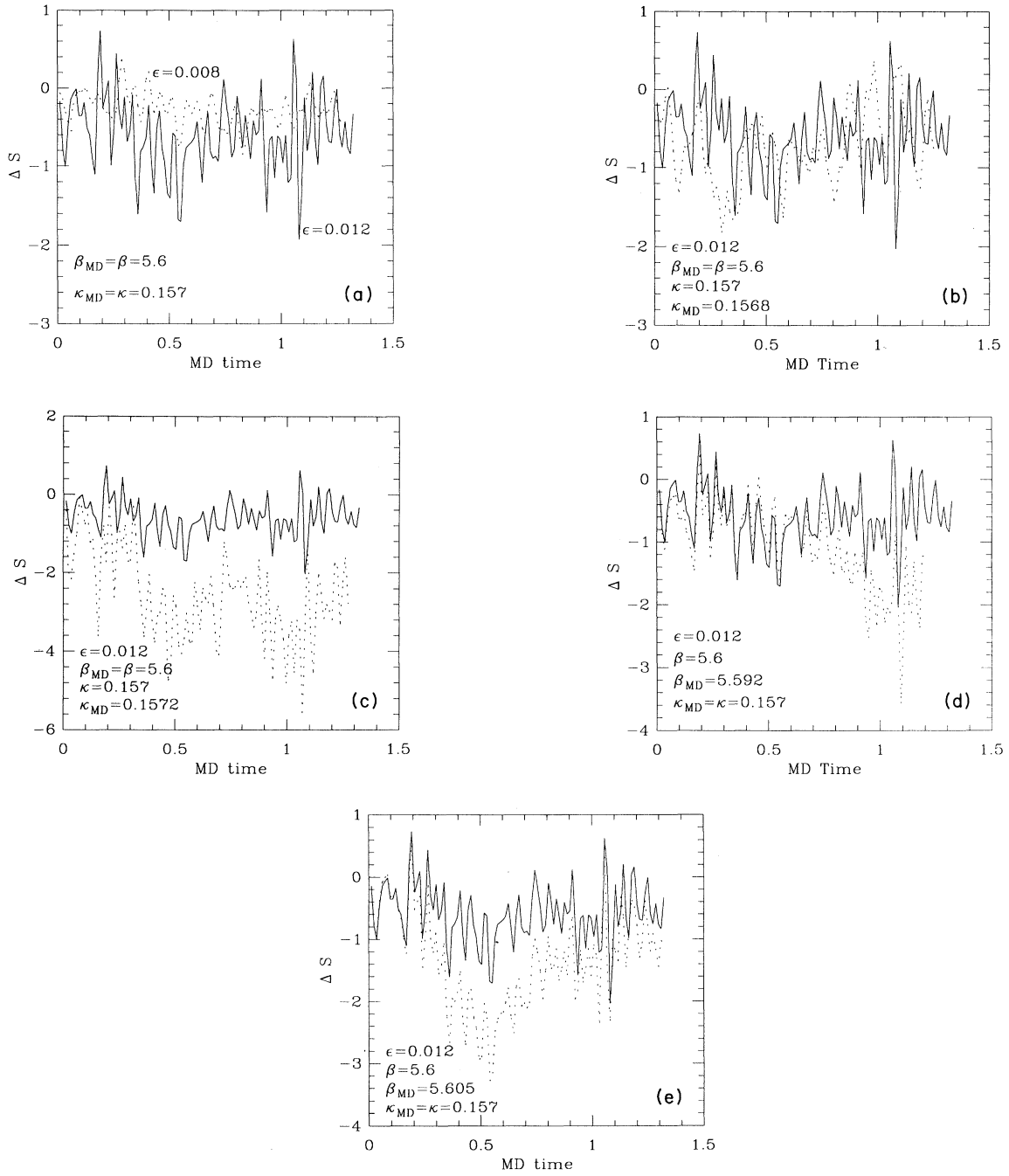

FIG. 1. (a) Change in the action, ΔS, as a function of the step size ϵ. The value of ϵ used in production runs is 0.009. (b) Comparing ΔS for $\kappa_{MD}<\kappa$ (dotted line) with the reference run $\kappa_{MD}=\kappa$ (solid line). In both runs $\beta_{MD}=\beta=5.6$ and $\epsilon=0.012$. (c) Same as (b) but with $\kappa_{MD}>\kappa$ (dotted line). (d) Comparing ΔS for $\beta_{MD}<\beta$ (dotted line) with the reference run $\beta_{MD}=\beta$ (solid line). In both runs $\kappa_{MD}=\kappa=0.157$ and $\epsilon=0.012$. (e) Same as Fig. (d) but with $\beta_{MD}>\beta$ (dotted line).

$\beta_{MD}=\beta$ and $\kappa_{MD}=\kappa$. We find this is the case for both Wilson and staggered fermions.

In Refs. [2] and [7] we carried out tests on 8^4 (Wilson) and up to $10^3\times4$ (staggered) lattices, respectively, and found that the performance of the HMC algorithm is improved if we set $\beta_{MD}<\beta$ and $\kappa_{MD}<\kappa$ (or $m_{q,Md}>m_q$). (This is true for the version of the leap-frog algorithm in which the gauge links are updated in the first half-step.) The qualitative change in our conclusions is a consequence of the increase in lattice volume. To keep the acceptance rate constant as the volume is increased, ϵ has to be decreased. In the molecular-dynamics evolution the leading-order effect of finite step size is a renormalization of the couplings in the action, the shifts being proportional to powers of ϵ. The tuning aims to undo the effect of these shifts and should therefore become less significant with increasing volume.

In Ref. [2], we proposed a scaling rule for critical slowing down of the HMC algorithm. The four factors that contribute, in the case of trajectories of length short compared to decorrelation time, are (a) the overall factor of lattice volume V, (b) the growth ($\propto 1/m_q$) in the number of iterations necessary to invert the Dirac operator, (c) the growth [$\propto(1/m_\pi^2)$] in the number of trajectories needed for a decorrelated lattice, and (d) the decrease in step size as $V^{-1/4}m_q^{3/2}$ to keep the acceptance rate fixed. Putting all these factors together, we estimated that in the worst case the computer time grows as $V^{5/4}m_q^{-7/2}$ for zero-temperature and large-volume simulations. A recent analysis by Gupta, Irbäck, Karsch, and Petersson [8] shows that the step size has to be decreased only as $V^{-1/4}m_q^{3/4}$. Even with this correction the computer power required to probe the chiral limit of QCD grows as $m_\pi^{-(4+2+2+1+1.5)}=m_\pi^{-10.5}$ with the present implementation of HMC algorithm. In arriving at this result we use $V\sim m_\pi^{-4}$ and take the pion to be the lightest mode with $m_\pi^2\propto m_q$. (Using the results in [2], the above estimate would change to m_π^{-10} for trajectories of length $O(1/m_\pi)$.) Thus QCD simulations with dynamical fermions still need a major breakthrough in update and matrix inversion algorithms.

III. DETAILS OF LATTICE UPDATE AND AUTOCORRELATIONS

The first 16^4 lattice we thermalized was at $\beta=5.5$ and $\kappa=0.159$ beginning from a hot start. We discarded 420 trajectories, of which the first 370 were run with the hybrid algorithm, i.e., without the accept-reject step. Thereafter thermalization at other values of the parameters consisted of taking a thermalized seed lattice and discarding 200 trajectories, of which the first 150 were run with the hybrid algorithm.

We have monitored the time history of up to 6×6 Wilson loops and hadron correlators in order to check if the HMC algorithm exhibits long autocorrelation times. In Fig. 2(a) we show the time history of 1×1, 2×2, and 3×3 loops at $\kappa=0.156$ and $\beta=5.6$ on 16^4 lattices for the post-thermalization part of the run. Long-distance observables such as the hadron correlators show similar behavior, as illustrated in Fig. 2(b) for the pion correlator. Such figures show that our present data sets are too short to determine autocorrelations accurately and that the autocorrelation times could easily be as large as a few hundred trajectories. We conclude that our initial lattices are reasonably thermalized, but that, given the total number of trajectories [see Table I(a)], our studies will be limited by small statistics. In our error analysis we do not include possible autocorrelations between configurations and we caution the reader that the errors are most likely underestimated.

Our initial updates of 16^4 lattices on the CM2 have the following error: the front-end random-number generator

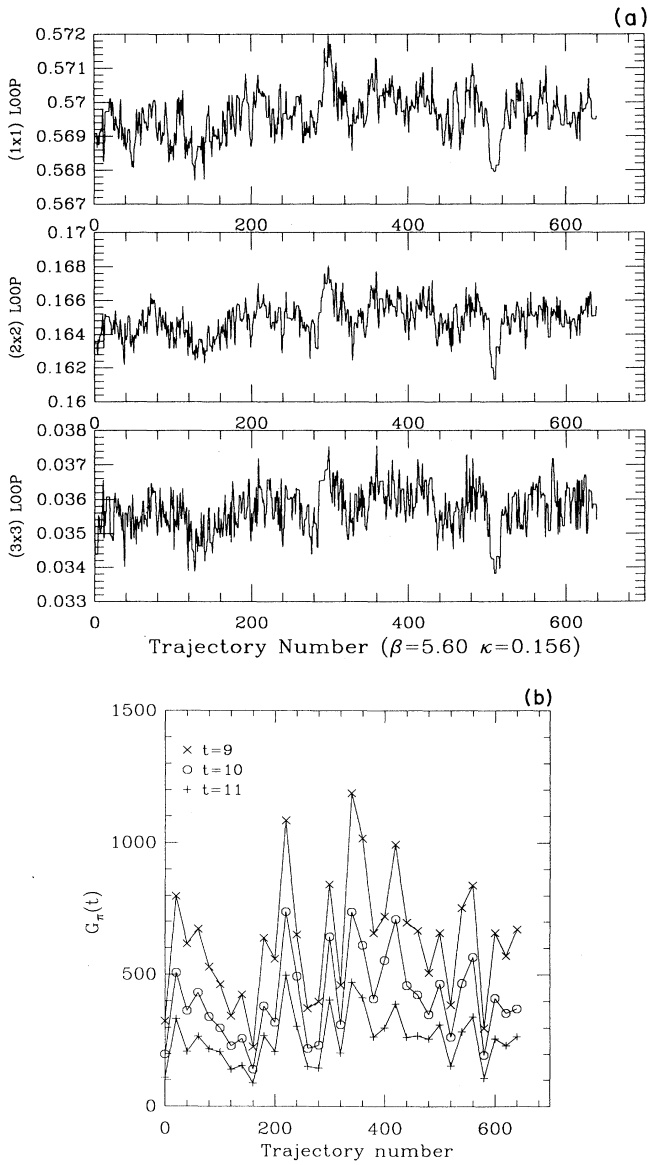

FIG. 2. (a) Time history of 1×1, 2×2, and 3×3 Wilson loops at $\beta=5.6$ and $\kappa=0.156$. (b) Time history of pion correlator at time separation 9, 10, and 11 at $\beta=5.6$ and $\kappa=0.156$. Points have been connected by a solid line to aid the eye.

(part of the *LISP package on the SUN) used in the crucial Metropolis accept-reject step was by default initialized with the same starting seed at the beginning of each restart of the job. Since a large fraction of the time a run consisted of a few trajectories, using the same random-number sequence is expected to produce a bias. Table I(a) shows the breakup of runs before and after we fixed the bug. So far we have not detected any significant difference in results between the two sets of runs. Since this problem only effects the accept-reject step, the update probably has errors similar to the step size errors in the simple hybrid algorithm, which are small for the values of ϵ used here. We estimate that the bias generated by using a random number of period 2–10 is at worst of the same order as the statistical errors.

We have begun generating $16^3\times 32$ lattices at the smaller quark masses. The status of this update is given in Table I(b), and we include only the Wilson loop data in the present analysis.

IV. WILSON LOOPS AND SCREENING IN THE $q\bar{q}$ POTENTIAL

The presence of light $q\bar{q}$ pairs in the QCD vacuum causes the flux tube between a heavy $q\bar{q}$ pair to break leading to the formation of two mesons. The interaction between these mesons is through a screened potential $V(r)\sim(1/r)\exp(-r/R_s)$, where R_s is the screening length. The distance scale at which the linear confining part is replaced by the screened potential will depend on the quark mass. Thus, as a first step to quantifying the effects of vacuum polarization it is necessary to demonstrate the vanishing of the linear confining part of the potential. At the same time we would also like to check if there is any change in the short-distance structure of the potential.

To calculate the $q\bar{q}$ potential, we have measured up to 6×6 Wilson loops in all the runs. These expectation values are given in Tables III, IV, and V for $\beta=5.4$, 5.5, and 5.6, respectively. From these we extract $V(r)$, the potential between a heavy $q\bar{q}$ pair, using

$$V(r)=\lim_{t\to\infty}\ln\left[\frac{W(r,t)}{W(r,t+1)}\right]. \tag{4.1}$$

The resulting data for $\beta=5.5$ are shown in Fig. 3.

TABLE III. Wilson loop data at $\beta=5.4$.

Size \ κ	0.1600	0.1610	0.1620
1×1	0.534 18(26)	0.537 97(20)	0.540 58(17)
1×2	0.308 67(34)	0.313 81(27)	0.317 53(24)
1×3	0.181 49(32)	0.186 42(26)	0.190 04(24)
1×4	0.107 16(26)	0.111 20(22)	0.114 22(20)
1×5	0.063 37(20)	0.066 38(17)	0.068 77(15)
1×6	0.037 48(15)	0.039 62(12)	0.041 37(12)
2×2	0.121 16(34)	0.126 28(28)	0.130 03(26)
2×3	0.051 08(24)	0.054 72(20)	0.057 47(19)
2×4	0.022 06(15)	0.024 22(13)	0.025 96(12)
2×5	0.009 58(10)	0.010 78(8)	0.011 80(8)
2×6	0.004 19(6)	0.004 82(5)	0.005 37(5)
3×3	0.016 69(14)	0.018 66(12)	0.020 31(12)
3×4	0.005 73(8)	0.006 66(7)	0.007 53(6)
3×5	0.001 99(5)	0.002 43(3)	0.002 85(4)
3×6	0.000 67(4)	0.000 87(3)	0.001 08(2)
4×4	0.001 68(5)	0.001 95(4)	0.002 37(4)
4×5	0.000 45(4)	0.000 64(2)	0.000 77(3)
4×6	0.000 11(4)	0.000 16(2)	0.000 27(2)
5×5	0.000 04(4)	0.000 16(3)	0.000 22(2)

TABLE IV. Wilson loop data at $\beta=5.5$.

Size \ κ	0.1580	0.1590	0.1600
1×1	0.554 83(10)	0.557 27(12)	0.560 33(4)
1×2	0.335 44(14)	0.338 90(16)	0.343 27(6)
1×3	0.206 83(14)	0.210 24(16)	0.214 65(7)
1×4	0.128 13(12)	0.131 02(14)	0.134 89(6)
1×5	0.079 45(10)	0.081 78(11)	0.084 87(5)
1×6	0.049 29(8)	0.051 06(8)	0.053 41(4)
2×2	0.146 36(16)	0.149 97(16)	0.154 73(7)
2×3	0.068 99(12)	0.071 79(13)	0.075 58(6)
2×4	0.033 24(9)	0.035 15(9)	0.037 82(5)
2×5	0.016 11(6)	0.017 35(6)	0.019 04(3)
2×6	0.007 84(4)	0.008 58(4)	0.009 62(2)
3×3	0.026 89(8)	0.028 72(10)	0.031 26(4)
3×4	0.011 01(5)	0.012 06(6)	0.013 59(3)
3×5	0.004 59(4)	0.005 17(4)	0.006 01(2)
3×6	0.001 90(3)	0.002 20(3)	0.002 70(2)
4×4	0.003 85(4)	0.004 45(5)	0.005 28(3)
4×5	0.001 37(4)	0.001 76(3)	0.002 11(2)
4×6	0.000 50(2)	0.000 67(2)	0.000 86(1)
5×5	0.000 42(3)	0.000 60(4)	0.000 77(1)
5×6	0.000 17(3)	0.000 23(2)	0.000 30(1)

TABLE V. Wilson loop data at $\beta=5.6$.

Size \ κ	0.1560	0.1570	0.1575
1×1	0.569 62(6)	0.571 46(4)	0.572 17(6)
1×2	0.354 66(8)	0.357 34(5)	0.358 33(8)
1×3	0.225 37(8)	0.228 10(6)	0.229 12(8)
1×4	0.143 91(8)	0.146 34(5)	0.147 24(8)
1×5	0.092 00(6)	0.094 00(4)	0.094 76(7)
1×6	0.058 83(5)	0.060 41(4)	0.061 02(5)
2×2	0.164 83(10)	0.167 88(6)	0.168 92(9)
2×3	0.082 91(8)	0.085 40(5)	0.086 25(8)
2×4	0.042 68(6)	0.044 47(4)	0.045 06(6)
2×5	0.022 15(4)	0.023 34(3)	0.023 71(4)
2×6	0.011 51(3)	0.012 27(2)	0.012 55(3)
3×3	0.035 69(6)	0.037 43(4)	0.038 05(6)
3×4	0.016 14(4)	0.017 24(3)	0.017 60(4)
3×5	0.007 43(2)	0.008 08(2)	0.008 30(3)
3×6	0.003 42(2)	0.003 81(1)	0.003 93(2)
4×4	0.006 58(3)	0.007 21(2)	0.007 41(3)
4×5	0.002 76(2)	0.003 11(1)	0.003 19(2)
4×6	0.001 16(1)	0.001 34(1)	0.001 39(2)
5×5	0.001 06(2)	0.001 23(1)	0.001 30(2)
5×6	0.000 43(1)	0.000 50(1)	0.000 53(1)
6×6	0.000 15(2)	0.000 20(1)	0.000 22(2)

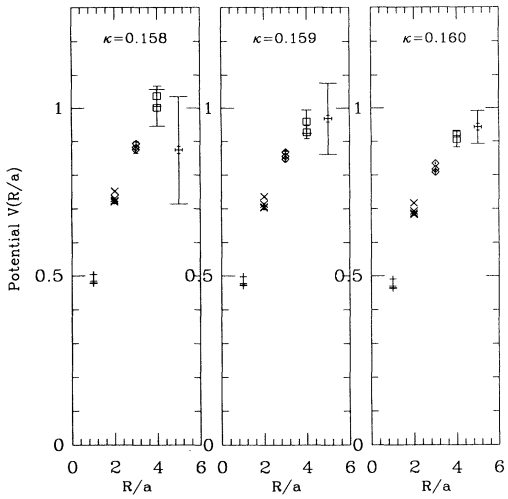

FIG. 3. The heavy $q\bar{q}$ potential $V(r)$ at $\beta=5.5$ and $\kappa=0.158$, 0.159, and 0.160. We use the same symbol at a given value of R/a for different values of t, and the data points show how the result converges from above as t is increased.

The data show that the asymptotic value of $V(r)$ is approached from above as $t\to\infty$ and only results for $r\leq 3$ have converged to better than 1%. In physical units, we have measured $V(r)$ for $r<0.5$ fm with the dynamical quark mass in the range $m_s<m_q<3m_s$. It is clear from Fig. 3 that we need data at larger values of r in order to test the onset of screening.

Plots of $V(r)$ at fixed β and r (e.g., Fig. 3) show a small decrease in the value of $V(r)$ as a function of κ. This trend is due to the decrease in the lattice scale a with increasing κ at fixed β and should not be interpreted as evidence for screening.

We have compared our results for the expectation values of Wilson loops (Tables III–V) to those from pure gauge theory. For every Wilson loop calculated in presence of dynamical fermions, we determine the matching β of the pure gauge theory that produces the same answer. The shifts $\Delta\beta$ are given in Table VI for Wilson loop data at $\beta=5.5$. If the only effect of dynamical fermions is an overall shift of the coupling β, then $\Delta\beta$ should be independent of the loop size at physical distances. On the other hand, if there is screening we expect $\Delta\beta$ to increase with loop area. The data show clearly that $\Delta\beta$ increases with loop area, and provide indirect evidence for screening.

TABLE VI. The difference in gauge coupling $\Delta\beta$ required to match $n_f=2$ Wilson loop data at $\beta=5.5$ with the pure gauge theory. For this matching we use a linear interpolation of pure gauge theory data.

Size \ κ	0.1580	0.1590	0.1600
1×1	0.231(4)	0.244(3)	0.260(2)
1×2	0.244(2)	0.259(1)	0.276(1)
1×3	0.250(1)	0.265(1)	0.283(1)
1×4	0.253(1)	0.267(1)	0.287(1)
1×5	0.255(1)	0.269(1)	0.289(1)
1×6	0.255(1)	0.271(1)	0.290(1)
2×2	0.261(1)	0.276(1)	0.296(1)
2×3	0.268(1)	0.284(1)	0.307(1)
2×4	0.271(1)	0.288(1)	0.313(1)
2×5	0.272(1)	0.291(1)	0.316(1)
2×6	0.273(1)	0.293(1)	0.319(1)
3×3	0.275(1)	0.294(1)	0.320(1)
3×4	0.279(1)	0.299(1)	0.326(1)
3×5	0.282(2)	0.304(2)	0.331(2)
3×6	0.282(3)	0.308(3)	0.346(7)
4×4	0.274(2)	0.302(3)	0.335(3)
4×5	0.277(5)	0.313(4)	0.341(7)
4×6	0.276(8)	0.315(8)	0.352(19)
5×5	0.266(10)	0.309(10)	0.340(15)

V. SMEARED QUARK PROPAGATORS

The positivity of the transfer matrix guarantees that for any interpolating field operator $\mathcal{O}$, the logarithmic rate of decrease of the two-point function $\langle\mathcal{O}\mathcal{O}\rangle$ will converge from above to the mass of the lightest state with the quantum numbers of $\mathcal{O}$. Thus, we can extract accurate mass estimates from lattice simulations if we can follow the signal in the two-point correlation functions for large enough time separations. In current calculations there are two sources of error: (a) statistics (the signal to noise ratio falls exponentially in all but the pion channel), and (b) the shortness of the lattice in the "time" direction (so that even if a signal exists, it cannot be followed far enough to extract the mass of the lowest state).

To reduce the second problem, we calculate the quark propagators on lattices doubled in the time direction, i.e., $16^3\times 16\to 16^3\times 32$. We use periodic boundary conditions in the update for both gauge and fermion fields. The calculation of quark propagators on doubled lattices also uses periodic boundary conditions in all four directions. Our data show that doubling allows us to follow the correlators long enough that the errors in the mass estimates are dominated by statistics.

In order to enhance the signal at large separation, we aim to maximize the overlap of the operator $\mathcal{O}$ with the wave function of the hadron being created. In this study, we use the Wuppertal source and sink method to calculate smeared quark propagators and to build hadron correlators out of them [9,10,6]. We use two types of smeared quark propagators in our calculation:

$$S_F^{SGS}(\mathbf{z},t;\mathbf{y},0)=\sum_{\mathbf{x},\mathbf{w}}K(\mathbf{z},t;\mathbf{w},t)G(\mathbf{w},t;\mathbf{x},0)\times K(\mathbf{x},0;\mathbf{y},0)\delta(\mathbf{y},0)\ ,$$
$$S_F^{GS}(\mathbf{z},t;\mathbf{y},0)=\sum_{\mathbf{x}}G(\mathbf{z},t;\mathbf{x},0)K(\mathbf{x},0;\mathbf{y},0)\delta(\mathbf{y},0)\ , \tag{5.1}$$

where G is the usual point-to-point Wilson fermion propagator and K is the inverse of the covariant Klein-Gordon operator in three dimensions. The lattice transcription we use is

$$K^{-1}(x;y)=\delta_{x,y}-\kappa_{\mathrm{KG}}\sum_{i=1}^{3}[U(x,i)\delta_{x+i,y}+U^{\dagger}(x,i)\delta_{x-i,y}]. \tag{5.2}$$

To obtain *SGS* and *GS* propagators we first smear the point source

$$\phi(\mathbf{x})=K(\mathbf{x};\mathbf{y})\delta(\mathbf{y}), \tag{5.3}$$

and then use ϕ as the source for the inversion of the Dirac equation. This yields the *GS* propagator; to get the *SGS* propagator we apply the inverse Klein-Gordon operator to *GS* on each time slice.

The hopping parameter κ_{KG} controls the size of the smearing and can be tuned to optimize the signal. We list the values of κ_{KG} used in the quark propagator calculations in Table VII. The size of the smearing is characterized by Ω which is defined on each configuration as

$$\Omega=\left[\frac{\sum_{\mathbf{x}} r^2|\phi(\mathbf{x})|^2}{\sum_{\mathbf{x}}|\phi(\mathbf{x})|^2}\right]^{1/2}. \tag{5.4}$$

For the data presented here we choose κ_{KG} as large as possible while keeping the fluctuations in Ω small, i.e., $\leq 10\%$. On our lattices we find that for $\Omega>5$ the norm of the hadron correlators fluctuates by orders of magnitude between configurations. Such large fluctuations would give rise to a poor statistical average, so the values of κ_{KG} were selected to give a smearing radius $\Omega\approx 4$. Even with this choice, the variation in the norm of the hadron correlators between configurations is, in some cases, as large as 5.

The Wuppertal smearing procedure is blind to the spin structure and is expected to work best in cases where the hadron wave function approximately factorizes as a product of quark and antiquark spatial wave functions. Within this approximation, the optimal Ω should roughly correspond to a typical hadronic size and one expects to improve the signal by tuning κ_{KG}.

A virtue of this smearing procedure is that only covariant derivatives are used, so that the final propagator (*SGS* or *GS*) has exactly the same gauge transformation property as that calculated with a point source. Thus, gauge-invariant hadron correlators are given by exactly the same expression in terms of the smeared propagator as in terms of the point propagator. For a further discussion of different types of quark sources and their relative merits, see Ref. [11].

TABLE VII. Parameters used in the calculation of quark propagators and the number of lattices analyzed.

β	$\kappa_d=\kappa_v$	κ_{KG}	Ω	N_{lattices}
5.4	0.160	0.187	4.1(2)	15
5.4	0.161	0.187	4.3(1)	15
5.4	0.162	0.184	4.0(2)	14
5.5	0.158	0.184	4.4(2)	15
5.5	0.159	0.184	4.3(1)	17
5.5	0.160	0.184	4.5(1)	27
5.6	0.156	0.181	4.1(2)	32
5.6	0.157	0.181	4.2(2)	45

The calculation of the quark propagators is done on Cray XMP's and YMP's, with the convergence criterion set to $R=10^{-14}$ for all lattice parameter values. To check that this criterion is sufficient, we increased the inversion accuracy to $R=10^{-15}$ on a few lattices at the smallest quark masses and compared results. We failed to detect any significant difference in the elements of quark propagator.

VI. HADRON SPECTRUM

The fitting procedure we use to extract the mass of the lowest state from the hadron correlator introduces a certain systematic error when the signal does not extend to very large separations. To control this systematic error, we first examine the effective mass plot for the existence of a stable plateau, and then make a single mass fit over this range of the plateau. We use the full covariance matrix in the fit, and the errors in the fit parameters are calculate using the single elimination jackknife method. We repeat this procedure dropping points from the plateau. In most cases, the χ^2/N_{DF} is of order 1 and is insensitive to the range of the fit, and we quote a result from the fit to the full plateau. The remaining cases almost always correspond to very small eigenvalues in the covariance matrix. In such cases we reduce the range of the fit to eliminate the small eigenvalues and to bring the χ^2/N_{DF} close to one. We find that fits using the covariance matrix typically give mass estimates that are 1σ higher than the case where correlations between time slices are neglected.

Using the above-stated procedure we extract masses of π, ρ, a_0, a_1, and b_1 mesons and both parity states of the N and Δ baryons. The effective mass plots for π, ρ, and nucleon at the lightest value of the quark mass are shown in Figs. 4 ($\beta=5.4$), 5 ($\beta=5.5$), and 6 ($\beta=5.6$). In these figures, the solid line gives the result obtained using a single mass fit to the points indicated. The dashed lines show the spread corresponding to the 1σ error obtained from the fit. This is to be compared with the variation in the effective mass over the range of the plateau as a consistency check. The range of the fit, the correlated χ^2/N_{DF}, and the final mass estimates are given in Tables VIII–X.

In Figs. 4–6 we compare the effective mass plots for both the *SGS* and the *GS* correlators. The errors in each point are calculated using single elimination jackknife. In nearly all cases the fits to the two different correlators gave results that are almost identical. The quality of the data is, however, different: the fluctuations in $m(t)$ for the *SGS* correlators are larger, while $m(t)$ from *GS* correlators takes one to two time slices longer to reach the plateau. Overall, the gain in overlap with the lightest state using *SGS* propagators is largely counterbalanced by a noisier signal. This conclusion is based on a comparison of signals from the *SGS* and the *GS* correlator on time slices from which the asymptotic mass is extracted

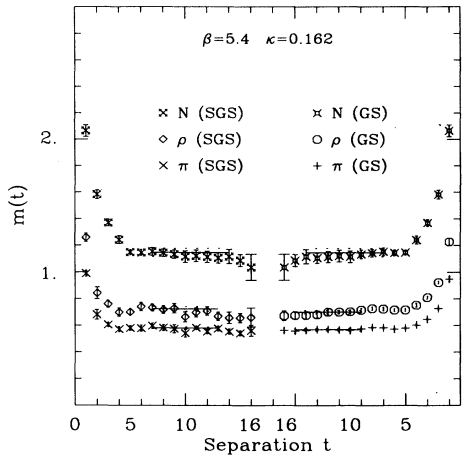

FIG. 4. Effective mass plot at $\beta=5.4$ and $\kappa=0.162$ for the pion, rho, and the nucleon. The data on the left-hand side are for the *SGS* correlator while that on the right (time reversed to ease comparison) are for the *GS* correlators.

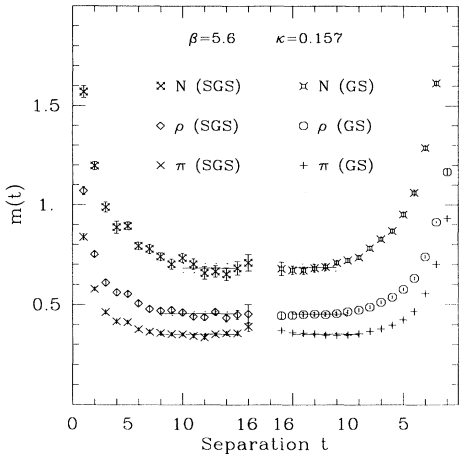

FIG. 6. Same as Fig. 4 but for $\beta=5.6$ and $\kappa=0.157$.

for the *GS* case. The cause of the extra noise is the additional smearing factors of K, which depend on the gauge fields on the sink time slice, in the functional average. Thus fluctuations of the gauge field, which are correlated between time slices, enhance the fluctuations in the hadron correlators. This effect correlates with the value of Ω on the individual configurations. Those having larger smearing size, and hence a larger norm for the correlators, dominate the statistical average. Therefore one cannot choose κ_{KG} too large and we find that Ω should not be much larger than 4 for our lattice parameters.

For the pion and rho we have looked at two different operators, and find that both give consistent results. We show a comparison using the $\beta=5.6, \kappa=0.157$ data with *SGS* correlators in Fig. 7. The operator $\pi_2 \equiv \gamma_4\gamma_5$ couples more strongly to the pion (the plateau is reached earlier), but the fluctuations in $m(t)$ are larger. For the ρ both operators have similar overlap with the state, though the signal is marginally better with the spin structure γ_i. Mass estimates using both operators for each set of values of β and κ and for both kinds of correlators are given in Tables VIII–X for the baryons we have averaged over the upper and lower Dirac components for each parity state.

The main drawback of the calculation presented here is that the plateau regions in the rho and nucleon effective mass plots have significant fluctuations (see Figs. 4–6) and errors of order 5% could easily be present in the mass estimates. These errors are due to poor statistics, especially in light of the large autocorrelation times we observe in the update.

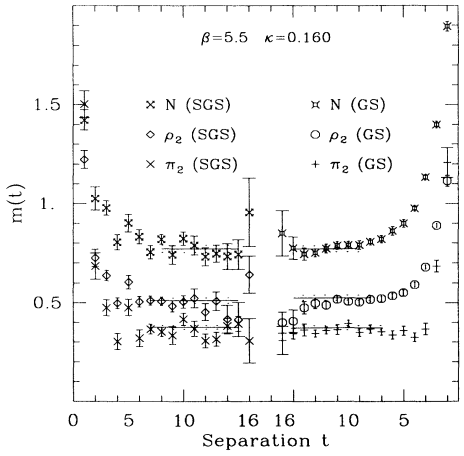

FIG. 5. Same as Fig. 4 but for $\beta=5.5$ and $\kappa=0.160$. We display data for operators π_2 and ρ_2 to show that their behavior is similar to that of π and ρ.

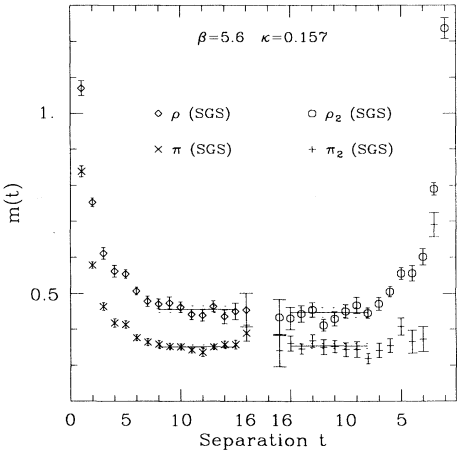

FIG. 7. Comparison of $m_{\text{eff}}(t)$ for the two pion and rho operators: $\pi \equiv \gamma_5$ versus $\pi_2 \equiv \gamma_4\gamma_5$ and $\rho \equiv \gamma_i$ versus $\rho_2 \equiv \gamma_4\gamma_i$. The data are from the *SGS* correlators at $\beta=5.6$ and $\kappa=0.157$.

Recently, the HEMCGC Collaboration reported seeing "wiggles" in the effective mass plots which they attribute to the use of the doubled (or quadrupled) lattices [12]. We find no evidence for such effects, so that, if present, they are smaller than our statistical errors. We should note however that our errors are larger than those of the HEMCGC Collaboration so there is as yet no contradiction.

We have only used one lattice size for each value of β and κ and therefore do not have a check on finite-size effects. Nevertheless, we expect that such effects are small for our quark masses, $m_q \geq m_s$, on our lattices of size 16^3. We expect this because in quenched calculations at a similar lattice spacing (e.g., $\beta \sim 6.0$) there is no evidence for finite-size effects in meson or baryon masses for $m_q \geq m_s$ on 16^3 lattices (e.g., see the data at $\beta = 6.0$ given in Tables V and VI of Ref. [13]). Now, finite-size effects come largely from pion loops that wind "around the world." These effects are present in both full and quenched theories, so we expect finite-size effects to be of similar magnitude. Note that at small quark masses the leading finite volume effect in a chiral expansion is absent in the quenched approximation for some mesons. For heavy quarks, however, this leading term is not dominant

We determine κ_c at each β by doing a linear fit of M_π^2 vs $1/\kappa$, and finding the value of κ at which M_π vanishes. Note that here we are holding $\kappa_{\rm val} = \kappa_{\rm dyn}$. The fits are shown in Figs. 8–10, and the resulting values of κ_c are listed in Table XI. To give a rough idea of the equivalent quenched theory we list the pure gauge couplings $\beta_{\rm eff}^{\kappa}$, which have the same κ_c as determined by interpolation of existing data.

TABLE VIII. (a) The meson spectrum at $\beta = 5.4$. Two kinds of hadron correlators are constructed: entries with label *S* are using *SGS* propagators and the other results are from *GS* correlators. The first number in each box is the correlated $\chi^2/N_{\rm DF}$ for the fit, the second is the range of the fit and the third is the mass estimate. (b) Baryon spectrum at $\beta = 5.4$. Notation as in (a).

κ_v	$\pi(\gamma_5)$	$\pi(\gamma_4\gamma_5)$	$\rho(\gamma_i)$	$\rho(\gamma_4\gamma_i)$	$a_1(\gamma_i\gamma_5)$	$a_0(1)$	$b_1(\epsilon_{ijk}\gamma_j\gamma_k)$
			(a)				
			$\kappa_d = 0.160$; 15 $12^4 \rightarrow 12^3 \times 24$ lattices				
	1.1	2.3	0.35	0.28	0.81	1.4	1.5
	5–11	5–11	5–11	5–11	3–6	3–6	3–6
0.160*S*	0.76(1)	0.79(2)	0.86(1)	0.87(1)	1.56(7)	1.60(10)	1.36(5)
			$\kappa_d = 0.161$; 15 $12^4 \rightarrow 12^3 \times 24$ lattices				
	1.2	0.80	1.0	0.85	1.1	1.7	0.94
	6–11	6–11	6–11	6–11	3–7	3–7	3–7
0.161*S*	0.69(2)	0.66(1)	0.78(1)	0.78(1)	1.20(5)	1.23(10)	1.14(5)
			$\kappa_d = 0.162$; 14 $16^4 \rightarrow 16^3 \times 32$ lattices				
	1.3	0.58	1.5	1.2	1.5	1.1	0.7
	7–13	9–15	7–13	7–13	4–8	4–8	4–8
0.162*S*	0.580(7)	0.569(10)	0.724(16)	0.724(16)	1.30(5)	1.24(8)	1.27(9)
	1.1	0.90	1.6	0.68	1.4	1.0	0.24
	7–13	7–13	9–15	7–13	4–9	4–9	4–9
0.162	0.574(10)	0.555(18)	0.703(13)	0.720(15)	1.21(5)	1.09(6)	1.20(6)

κ_v	N^+	N^-	Δ^+	Δ^-
		(b)		
	$\kappa_d = 0.160$; 15 $12^4 \rightarrow 12^3 \times 24$ lattices			
	0.59	0.3	0.47	0.93
	2–8	3–8	2–8	3–7
0.160*S*	1.45(3)	1.98(7)	1.52(3)	1.93(14)
	$\kappa_d = 0.161$; 15 $12^4 \rightarrow 12^3 \times 24$ lattices			
	0.84	0.68	1.1	1.4
	4–9	3–7	4–9	3–7
0.161*S*	1.31(3)	1.58(4)	1.40(4)	1.71(9)
	$\kappa_d = 0.162$; 14 $16^4 \rightarrow 16^3 \times 32$ lattices			
	0.55	0.40	0.59	1.3
	6–12	4–8	7–13	4–8
0.162*S*	1.15(2)	1.59(3)	1.26(3)	1.53(6)
	0.18	0.5	0.1	1.0
	7–14	4–8	7–12	4–8
0.162	1.15(3)	1.58(4)	1.25(3)	1.63(4)

Having determined κ_c, the masses for all other states are extrapolated to κ_c using linear fits of M vs $1/\kappa$. These fits are also shown in Figs. 8–10. We estimate the lattice scale $1/a$ comparing the extrapolated M_ρ and M_N to the experimental values. The resulting scales are listed in Table XI. We should add a word of caution that linear fits are expected to be particularly unreliable for M_ρ, as significant curvature may be present at the two-pion threshold [14].

In Figs. 8–10 we also show f_π/Z_A^L calculated on the

TABLE IX. (a) Meson spectrum at $\beta=5.5$. Notation as in Table VIII (a). (b) Baryon spectrum at $\beta=5.5$. Notation as in Table VIII (a).

κ_v	$\pi(\gamma_5)$	$\pi(\gamma_4\gamma_5)$	$\rho(\gamma_i)$	$\rho(\gamma_4\gamma_i)$	$a_1(\gamma_i\gamma_5)$	$a_0(1)$	$b_1(\epsilon_{ijk}\gamma_j\gamma_k)$
			(a)				
			$\kappa_d=0.158;15$ $16^4\rightarrow 16^3\times 32$ lattices				
	0.47	0.65	0.13	1.2	1.2	2.1	1.7
	6–13	6–13	6–13	6–13	3–8	3–8	3–8
0.158*S*	0.567(5)	0.569(8)	0.672(8)	0.672(9)	1.10(4)	1.07(4)	1.12(5)
	0.78	0.42	0.57	0.55	0.1	1.3	1.8
	8–14	8–14	8–14	8–14	5–9	4–9	4–9
0.158	0.568(5)	0.569(7)	0.672(9)	0.672(9)	1.11(3)	1.08(5)	1.15(3)
			$\kappa_d=0.159;$ 17 $16^4\rightarrow 16^3\times 32$ lattices				
	0.77	0.79	0.94	0.68	2.0	0.47	2.6
	6–14	6–14	6–14	6–14	3–8	3–8	3–8
0.159*S*	0.480(4)	0.480(5)	0.598(8)	0.599(9)	1.11(4)	1.04(5)	1.06(4)
	0.54	0.89	0.82	1.6	0.38	1.2	0.75
	6–14	6–13	6–14	8–14	3–8	3–8	3–8
0.159	0.473(6)	0.476(8)	0.593(6)	0.607(7)	1.07(2)	1.02(3)	1.06(2)
			$\kappa_d=0.160;$ 27 $16^4\rightarrow 16^3\times 32$ lattices				
	0.76	1.3	0.78	0.72	4.1	1.6	0.81
	8–15	7–15	8–15	7–15	4–8	4–8	4–8
0.160*S*	0.350(10)	0.376(9)	0.518(15)	0.513(14)	0.81(5)	0.79(6)	0.94(6)
	1.4	1.3	0.42	2.5	2.6	1.4	1.4
	9–15	7–15	9–14	8–16	7–12	7–12	7–12
0.160	0.363(12)	0.374(11)	0.516(10)	0.527(13)	0.70(9)	0.70(12)	0.84(8)

κ_v	N^+	N^-	Δ^+	Δ^-
		(b)		
	$\kappa_d=0.185;$ 15 $16^4\rightarrow 16^3\times 32$ lattices			
	0.30	0.68	0.31	1.2
	6–13	4–10	6–13	4–9
0.158*S*	1.10(2)	1.49(5)	1.17(3)	1.68(10)
	0.06	0.48	0.48	0.77
	7–13	6–10	7–13	6–10
0.158	1.09(2)	1.44(6)	1.16(2)	1.59(7)
	$\kappa_d=0.159;$ 17 $16^4\rightarrow 16^3\times 32$ lattices			
	0.81		0.74	
	6–14		6–14	
0.159*S*	0.94(2)		1.02(2)	
	0.34	0.87	1.1	0.78
	6–11	6–9	6–11	6–9
0.159	0.96(3)	1.27(8)	1.07(3)	1.41(9)
	$\kappa_d=0.160;$ 27 $16^4\rightarrow 16^3\times 32$ lattices			
	0.77	0.22	1.4	1.5
	8–15	6–10	8–15	6–10
0.160*S*	0.77(2)	0.98(6)	0.88(3)	1.17(12)
	1.2	0.70	0.92	0.12
	9–15	7–12	9–15	7–12
0.160	0.77(2)	1.06(6)	0.88(2)	1.25(11)

TABLE X. (a) Meson spectrum at $\beta=5.6$. Notation as in Table VIII (a). (b) Baryon spectrum at $\beta=5.6$. Notatin as in Table VIII (a).

κ_v	$\pi(\gamma_5)$	$\pi(\gamma_4\gamma_5)$	$\rho(\gamma_i)$	$\rho(\gamma_4\gamma_i)$	$a_1(\gamma_i\gamma_5)$	$a_0(1)$	$b_1(\epsilon_{ijk}\gamma_j\gamma_k)$
			(a)				
			$\kappa_d=0.156$; 32 $16^4\rightarrow 16^3\times 32$ lattices				
	0.78	1.1	0.86	0.70	1.1	1.1	2.0
	8–15	8–15	8–15	8–15	5–10	5–10	5–10
0.156*S*	0.463(5)	4.463(7)	0.55(1)	0.55(1)	0.84(2)	0.84(3)	0.87(3)
	1.6	3.0	1.2	1.5		1.0	
	9–15	9–15	9–15	9–15		5–10	
0.156	0.451(6)	0.458(7)	0.55(1)	0.55(1)		0.85(3)	
			$\kappa_d=0.157$; 45 $16^4\rightarrow 16^3\times 32$ lattices				
	0.63	0.46	0.74	1.2	1.1	0.31	0.52
	8–15	8–15	8–15	8–15	3–8	3–8	3–8
0.157*S*	0.352(5)	0.355(7)	0.456(10)	0.447(14)	0.85(2)	0.76(2)	0.87(2)
	0.81	1.5	0.53	0.96	1.4	0.73	0.15
	9–15	9–15	10–15	9–15	5–10	5–10	5–10
0.157	0.352(5)	0.358(7)	0.454(9)	0.441(9)	0.83(2)	0.75(3)	0.87(2)

κ_v	N^+	N^-	Δ^+	Δ^-
	(b)			
	$\kappa_d=0.156$; 32 $16^4\rightarrow 16^3\times 32$ lattices			
	0.28	0.1	0.19	1.3
	8–14	7–12	8–14	7–12
0.156*S*	0.87(2)	1.11(6)	0.91(2)	1.18(7)
	0.86	1.6	1.6	1.5
	9–15	7–12	9–15	7–12
0.156	0.87(2)	1.18(3)	0.93(3)	1.24(4)
	$\kappa_d=0.157$; 45 $16^4\rightarrow 16^3\times 32$ lattices			
	0.64	0.86	0.34	0.51
	10–15	6–11	10–15	7–11
0.157*S*	0.68(2)	1.08(3)	0.74(2)	1.05(7)
	0.65	0.66	1.4	0.66
	11–15	7–11	11–15	7–11
0.157	0.69(2)	1.10(3)	0.77(2)	1.16(4)

same set of lattices [4]. We find that a linear extrapolation in $1/\kappa$ gives a good fit to the data. We use this extrapolated value to give a third estimate of the lattice scale in Table XI.

The key physics question in any spectrum calculation is the behavior of the ratio M_N/M_ρ as a function of the quark mass. We show the APE Collaboration mass plot of our $n_f=2$ data in Fig. 11, and compare it with the best quenched data for Wilson fermions at $\beta=6$ in Fig. 12 [15]. To guide the eye we also give two phenomenological parametrizations: the solid line for $M_\pi/M_\rho>0.7$ in the figures is derived using a potential model based on hyperfine interactions [16] while the second solid line is the linear term in a chiral expansion [17]. There is, how-

TABLE XI. The chiral limit κ_c is determined using linear extrapolation of M_π^2 data at each of the three values of β. The lattice scale is determined using a linear extrapolation for M_ρ, M_N, and f_π/Z_A^L to κ_c, and then fixing $M_\rho=770$ MeV, $M_N=938$ MeV and $f_\pi=132$ MeV. We use $Z_A^L=0.86$. For comparison we also list the pure gauge couplings that have approximately the same κ_c and a rough estimate of κ corresponding to the strange quark.

		Lattice scale and κ_c for $n_f=2$ Wilson fermions				
β	κ_c	$\beta_{\rm eff}^{\kappa}$	$1/a$ (GeV)	$1/a$ (GeV)	$1/a$ (GeV)	$\kappa(m_s)$
			(M_ρ)	(M_N)	(f_π)	
5.4	0.164 50	5.718	1.45(10)	1.2(1)	1.5(3)	0.163
5.5	0.161 45	5.858	1.9(1)	1.7(1)	1.8(2)	0.160
5.6	0.158 53	5.95	2.6(3)	2.3(4)	2.3(4)	0.1576

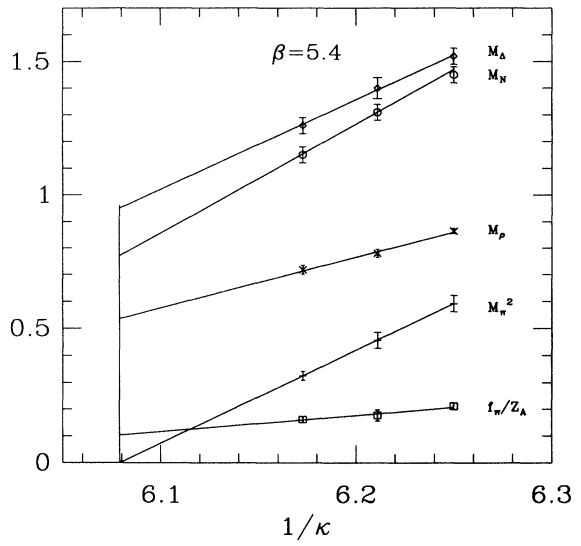

FIG. 8. The mass spectrum at $\beta=5.4$ as a function of $1/\kappa$. The solid lines are a linear fit to the data and extrapolated to κ_c.

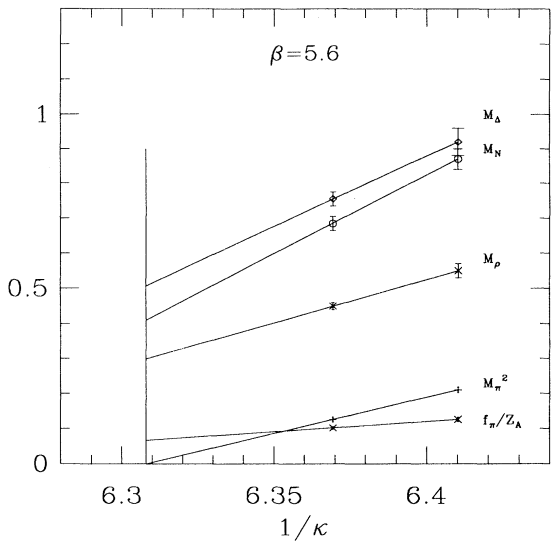

FIG. 10. Same as Fig. 8 but at $\beta=5.6$.

ever, an important caveat in using these curves as a guide: in our data we hold $\kappa_{\rm val}=\kappa_{\rm dyn}$ while the curves correspond to holding the mass of the sea quarks fixed at their physical value and varying just the valence quark mass.

The ratio $M_\pi/M_\rho=0.7$ corresponds roughly to $m_q=m_s$ [18]. In Table XI we give a rough estimate of the value of κ corresponding to m_s for each of the three values of β. We see that our $n_f=2$ data falls in the range $m_s<m_q<3m_s$, and that it is roughly consistent with both the quenched results and the potential model. To see substantial effects of fermion loops will certainly require better statistics and will most likely require smaller quark masses.

The data show a clear increase in the mass splitting between the nucleon and the Δ as the quark mass is lowered. In the nonrelativistic quark model (NRQM), this splitting is due to the hyperfine interactions and is expected to scale as $(1/m^2_{\rm constituent})$. Our lattice data qualitatively reproduce the effect as shown in Fig. 13 where we plot the splitting in baryons versus that for mesons [19]. We also find that the $n_f=2$ data is in good agreement with quenched results.

It is interesting to make a detailed comparison of our results at $\beta=5.6$ with those for the quenched spectrum at $\beta=6.0$ The latter, which are collected in Table XII,

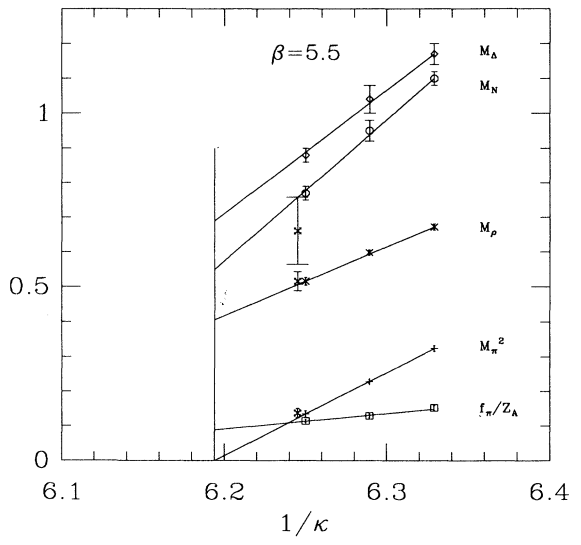

FIG. 9. Same as Fig. 8 but at $\beta=5.5$. The points labeled with a fancy cross at $\kappa=0.160$ are from Ref. [21].

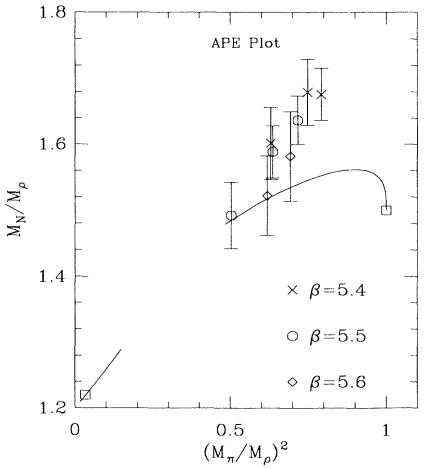

FIG. 11. APE plot for the $n_f=2$ theory based on spectrum data presented in Tables VIII–X.

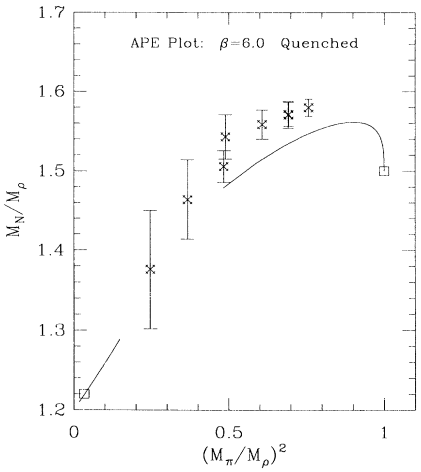

FIG. 12. APE plot for the quenched spectrum data at $\beta=6.0$ given in Table XII.

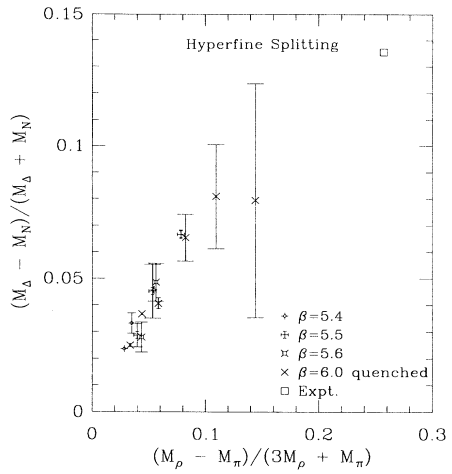

FIG. 13. Comparison of hyperfine splitting between the nucleon and the Δ versus that between the ρ and the π. We show both our $n_f=2$ data and quenched results at $\beta=6.0$.

come from (a) the APE Collaboration (using a multicube source) [15], and (b) our results on $16^3\times40$ quenched lattice (using a Wuppertal source with $\Omega\sim4$) [20]. We note that our results are in reasonable agreement with those of APE. There is a 2σ discrepancy in the Δ mass, which may be an artifact of the different fitting procedures, combined with some finite-size effects at $\kappa=0.155$.

We find that there is a reasonably good match between the $\kappa=0.157$ dynamical data and the $\kappa=0.154$ quenched results, and between $\kappa=0.156$ dynamical and $\kappa=0.152$ quenched. What is clear from this comparison is that $\partial M/\partial(1/2\kappa)$ is about twice as large for the $n_f=2$ theory as compared to the quenched case. We will come back to this point in Sec. VII when we discuss the pion-nucleon σ term.

The only earlier calculation we can compare our results against is that of Fukugita and Ukawa at $\beta=5.5$ and $\kappa=0.16$ [21]. They used a second-order Langevin algorithm to update $9^3\times18$ lattices and calculated the spectrum for three different step sizes. The zero step size limit was determined using a linear extrapolation. We show their results in Fig. 9 and for clarity displace them slightly from $\kappa=0.16$. The pion and rho masses are in agreement, and the errors in their estimate of the nucleon mass are too large to make a useful comparison. The errors in our data are considerably smaller, which we attribute to the use of smeared sources and a larger spatial volume.

VII. SCALAR DENSITY AND AXIAL-VECTOR MATRIX ELEMENTS

The matrix elements of quark bilinear operators, $\bar{q}\Gamma q$, where Γ is a Dirac matrix, in hadronic states are simple probes of the physics of QCD. They occur in parametrizations of hadronic mass splittings, semileptonic-decay

TABLE XII. Quenched Wilson fermion spectrum at $\beta=6.0$. The results on $18^3\times32$ and on $24^3\times32$ lattices are from the APE Collaboration.

κ	Lattice	Configs.	π	ρ	N	Δ
0.152	$18^3\times32$	104	0.474(1)	0.545(2)	0.861(5)	0.905(6)
0.153	$18^3\times32$	104	0.420(1)	0.504(3)	0.792(6)	0.843(7)
0.153	$24^3\times32$	78	0.423(2)	0.509(2)	0.805(6)	0.87(1)
0.154	$16^3\times40$	35	0.365(4)	0.465(7)	0.736(11)	0.82(2)
0.154	$18^3\times32$	104	0.361(1)	0.463(3)	0.721(7)	0.782(10)
0.155	$16^3\times40$	35	0.301(6)	0.420(12)	0.663(15)	0.78(2)
0.155	$18^3\times32$	104	0.295(1)	0.422(4)	0.651(10)	0.723(14)
0.155	$24^3\times32$	78	0.297(3)	0.428(4)	0.647(6)	0.745(15
0.1558	$24^3\times32$	78	0.234(5)	0.397(7)	0.57(1)	0.67(3)
0.1563	$24^3\times32$	78	0.186(7)	0.377(9)	0.52(2)	0.61(6)

amplitudes, lepton-hadron scattering cross sections etc. Of particular interest are the matrix elements which vanish in the NRQM, e.g., the strange-quark matrix elements of the proton $\langle P|\bar{s}\Gamma s|P\rangle$. They are crucial for understanding a number of open questions such as the pion-nucleon σ term (S:$\Gamma=1$), the spin content of the proton and polarized muon-proton scattering data (A:$\Gamma=i\gamma_\mu\gamma_5$) and the θ dependence of the neutron electric dipole moment (Θ:$\Gamma=i\gamma_5$).

Each quark bilinear matrix element consists of the two contributions shown in Fig. 14. Figure 14(a) shows the insertion on the "valence" quarks, while Fig. 14(b) is the contribution from insertion on the "sea" quarks. In the limit of exact flavor symmetry, flavor-nonsinglet matrix elements are given entirely by the valence contribution. The sea-quark contribution is, however, an essential part of flavor-singlet matrix elements; in fact it is the only contribution to matrix elements such as $\langle P|\bar{s}\Gamma s|P\rangle$. Lattice technology is sufficiently well developed for a reliable calculation of the valence contribution, and encouraging results have been obtained in the quenched approximation [22,23,9,24]. The calculation of the sea-quark piece is more difficult, for two reasons. First, it requires an insertion on the vacuum loop, which is a technical challenge. Second, this insertion must then be correlated with the hadron propagator, a correlation occurring by multiple-gluon exchange and hence noisy. One way to calculate the sea contribution is to generate the disconnected piece using pseudofermions. In our previous attempt [25] we obtained a poor signal with this method, and we have not attempted the calculation here. The only instance in which we can estimate the sea-quark contribution is for the scalar insertion, as we describe shortly.

The flavor-nonsinglet matrix elements can be extracted from the ratio of three- to two-point correlation functions. We consider here only the scalar and axial-vector insertions. We use the method of Refs. [22] and [9], inserting the source at zero four-momentum and picking out the term linear in t:

$$\frac{\sum_{\mathbf{x}}\left\langle \mathcal{P}_\alpha(\mathbf{x},t)\sum_{z}\bar{q}(z)\Gamma q(z)\mathcal{P}^\dagger_\beta(\mathbf{0},0)\right\rangle}{\frac{1}{2}\sum_{\delta=1}^{2}\sum_{\mathbf{x}}\langle \mathcal{P}_\delta(\mathbf{x},t)\mathcal{P}^\dagger_\delta(\mathbf{0},0)\rangle} \underset{t\to\infty}{\sim} \text{const}+t\Gamma_{\alpha\beta}\frac{f\langle P|(\bar{q}\Gamma q)^{\text{cont}}|P\rangle}{Z^L_\Gamma} . \quad (7.1)$$

Here $\mathcal{P}_\alpha(\mathbf{x},t)$ is the interpolating field for the proton. For a proton propagating forward in time with $\mathbf{p}=0$, the Dirac indices (α,β,δ) are restricted to be 1 or 2. To improve the statistical accuracy we combine them with Dirac indices 3 and 4 corresponding to an antiproton propagating backward in time. Some subtleties in the derivation of Eq. (7.1) are discussed in Appendix B. We only note here that (1) the factor of f takes into account some of the $O(a)$ corrections, and, in particular, gives the formula the correct limit as $\kappa\to 0$, and (2) the Z factors relate the lattice and continuum operators.

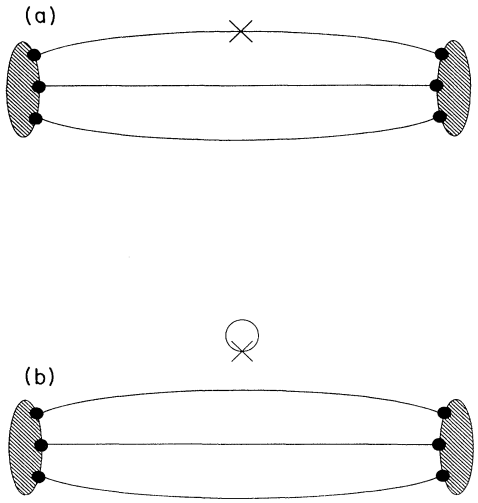

FIG. 14. The two kinds of insertions that contribute to the matrix elements of quark bilinear operators such as the scalar density and the axial-vector current.

To calculate the scalar and axial-vector matrix elements we use the standard source technique to insert the bilinear operators on the quark propagators [22]. Both scalar and axial-vector insertions can be done simultaneously using the Hermition matrix $\Gamma=(1+i\sum_i\gamma_i\gamma_5)$. This combination contains all the four linearly independent components that survive in the NRQM limit, and the individual matrix elements can easily be projected out from Eq. (7.1). We use the following notation. The matrix elements of $(\bar{u}\Gamma u-\bar{s}\Gamma s)$ inside a proton, ρ^+ and Δ^{++} are denoted by $2F_\Gamma$, ρ_Γ, and Δ_Γ, respectively. The proton matrix element of $(\bar{u}\Gamma u-2\bar{d}\Gamma d+\bar{s}\Gamma s)$ gives $2D_\Gamma$. We stress that by neglecting the contractions shown in Fig. 14(b) we are working in the SU(3) limit in which the sea graphs cancel. Table XIII gives the experimental values [26] and the infinite quark mass limit for these matrix elements.

We extract the matrix elements from a fit to the linear

TABLE XIII. The experimental numbers for the nonsinglet scalar density and axial-vector current matrix elements are extracted assuming first-order flavor-SU(3)-symmetry breaking. The symmetry-breaking-mass term $m_{SB}=m_s-0.5\times(m_u+m_d)$ is expressed in MeV.

	F_S	D_S	F_A	D_A	ρ_S	Δ_S
$m_q=\infty$	1	0	2/3	1	1	3
Expt.	$190/m_{SB}$	$-61/m_{SB}$	0.47(4)	0.81(3)	$124/m_{SB}$	$440/m_{SB}$

term in Eq. (7.1). The errors are calculated using a single elimination jackknife procedure. For each jackknife sample the covariance matrix for calculating the $\chi^2/N_{\rm DF}$ used in the fit is constructed directly for the ratio $\mathcal{R}(t)\equiv\langle x(t)\rangle/\langle y(t)\rangle$, using the formula

$$V_{i,j}=\frac{1}{N}\sum_{n=1}^{N}\delta\mathcal{R}_i^n\delta\mathcal{R}_j^n\ , \tag{7.2}$$

where the index n runs over the configurations and i,j over the range of times slices to which the fit is made. For the ratio of correlators, the differential $\delta\mathcal{R}_i^n$ is taken to be

$$\delta\mathcal{R}_i^n=\mathcal{R}_i\left[\frac{x_i^n-\langle x_i\rangle}{\langle x_i\rangle}-\frac{y_i^n-\langle y_i\rangle}{\langle y_i\rangle}\right]\ . \tag{7.3}$$

We find that the ratio in Eq. (7.1) shows linear behavior from an earlier time than that at which the lowest-mass state saturates the individual correlation functions. In Table XIV we give the results of the fits, together with the range of t over which we make linear fits, and the $\chi^2/N_{\rm DF}$. We show examples of plots of the ratios of correlators from which F_S, D_S, F_A, and D_A are extracted in Figs. 15(a), 15(b), 15(c), and 15(d), respectively. The quality of the signal in all quantities except D_s is similar, and one can make reliable fits keeping 5–6 time slices. The data for D_S is poor, especially at the heavier-quark masses where $D_S\sim 0$.

In order to evaluate whether vacuum-polarization effects play any role for $m_q > m_s$, we repeat the analysis on the quenched $16^3\times 40$ lattices [20]. The results, which are of similar quality as for the unquenched lattices, are given in Table XV.

We begin by discussing the axial-vector matrix elements F_A and D_A, which have the smallest errors. These were first calculated in Ref. [9], with results that interpolated well between the infinite-quark mass and experimental values. Most of the change in $g_A\equiv F_A+D_A$ oc-

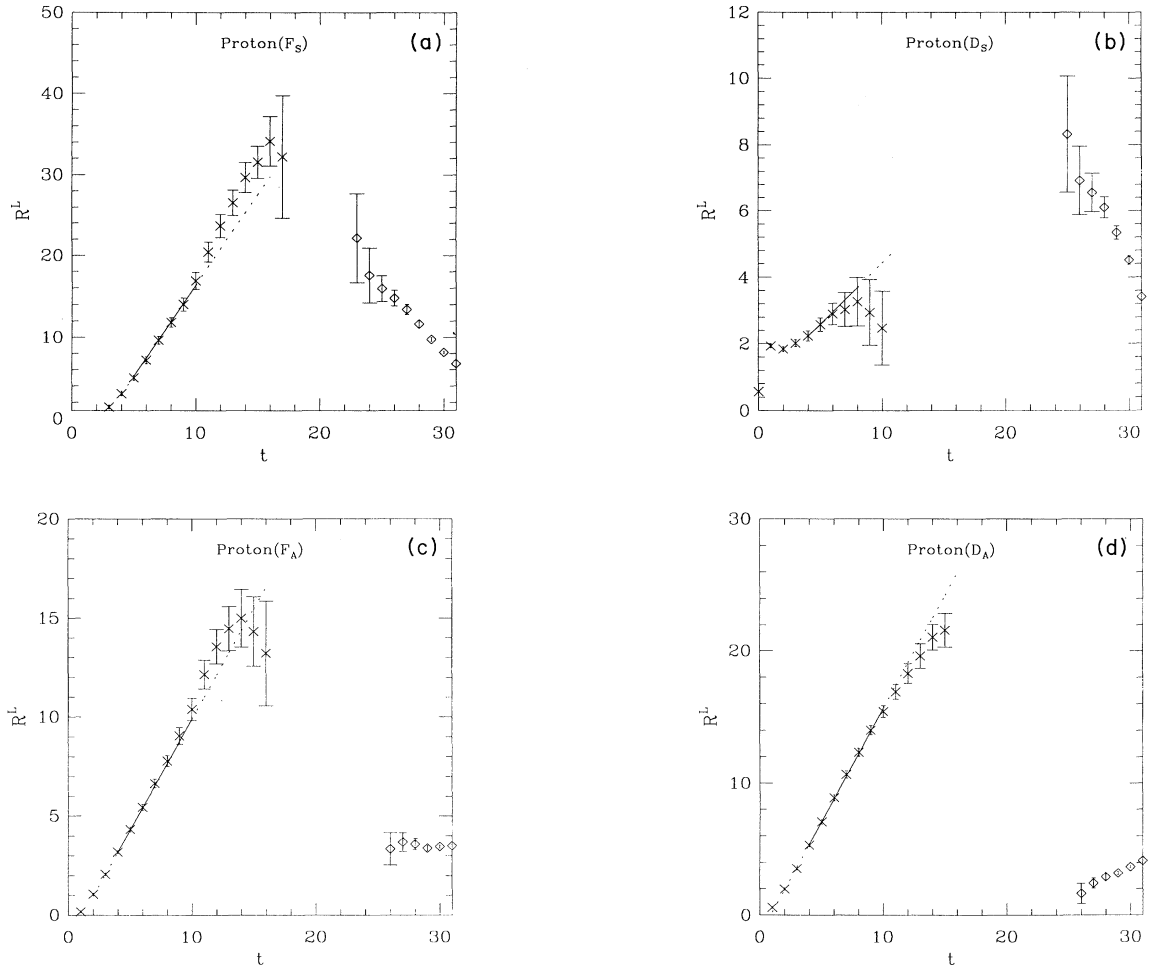

FIG. 15. (a) Plot of the ratio of three-point function to the two-point correlator from which the reduced matrix element F_S is extracted using the form given in Eq. (7.1). The data are from $\beta=5.6$ and $\kappa=0.157$ lattices. The points labeled with symbol $\times$ are for the proton and those with $\diamond$ are for the opposite parity nucleon. (b) Same as (a) except that the data are for D_S. (c) Same as (a) except that the data are for F_A. (d) Same as (a) except that the data are for D_A.

curred for $M_\pi/M_\rho > 0.8$, below which the results were consistent with the experimental numbers. Our results lie in the range $0.7 < M_\pi/M_\rho < 0.88$ and show little variation with mass. This lack of variation is confirmed by the fact that the quenched results of Ref. [24] at $\beta=6$, $\kappa=0.152$ agree with our quenched results at larger κ. Furthermore, the results depend little on β, or on the use of the quenched approximation. This all suggests that

TABLE XIV. Nonsinglet scalar density and axial-vector current matrix elements at $\beta=5.4$, 5.5, and 5.6. The renormalization constant Z_Γ^L have not been determined for these lattices. An estimate based on perturbation theory and quenched calculations is $Z_A^L/f \sim 0.86$. No numbers are given where the signal is poor and the notation is as in Table VIII (a).

β	κ	fF_s/Z_S^L	fD_s/Z_S^L	fF_A/Z_A^L	fD_A/Z_A^L	$f\rho_s/Z_S^L$	$f\Delta_s/Z_S^L$
		1.1	2.0	0.50	0.51	0.98	1.9
		3–7	2–7	3–7	3–7	3–7	3–7
5.4	0.160*S*	0.81(4)	−0.08(3)	0.54(3)	0.81(4)	0.75(4)	1.9(2)
		31.0	0.37	13.6	19.0	0.81	11.0
		3–9	2–7	3–9	3–9	3–7	3–7
5.4	0.161*S*	0.87(3)	−0.04(2)	0.57(2)	0.86(5)	0.77(3)	2.2(2)
		0.67		0.75	0.47	2.6	1.0
		3–8		3–8	3–8	3–9	3–8
5.4	0.162*S*	0.99(3)		0.55(3)	0.83(4)	0.79(3)	2.9(1)
		0.38	0.43	0.98	1.2	2.5	1.7
		4–9	5–9	4–9	4–9	4–9	4–9
5.4	0.162	1.02(5)	−0.16(9)	0.56(3)	0.85(2)	0.79(3)	2.7(1)
			1.6	2.3	2.3		4.3
			3–8	3–8	3–8		5–12
5.5	0.158*S*		−0.06(3)	0.55(3)	0.85(2)		2.4(1)
		1.5	2.6	1.5	2.2	8.0	0.23
		6–12	4–10	6–12	6–12	5–13	6–12
5.5	0.158	0.96(5)	−0.05(3)	0.56(3)	0.88(2)	0.85(6)	2.5(2)
		1.0	2.2	2.3	0.95	1.2	0.75
		5–10	4–8	4–8	4–8	5–10	4–8
5.5	0.159*S*	1.13(7)	−0.08(4)	0.59(3)	0.87(1)	0.83(7)	2.6(3)
		0.85	0.82	0.49	1.4	1.1	1.4
		5–10	4–8	4–8	4–8	5–10	4–8
5.5	0.159	1.10(5)	−0.15(4)	0.58(2)	0.85(2)	0.88(6)	2.5(2)
		0.39	0.99	3.1	0.13	1.4	0.45
		6–11	4–10	4–9	4–9	5–12	4–10
5.5	0.160*S*	1.04(12)	−0.36(7)	0.55(5)	0.81(3)	0.77(7)	2.0(3)
		0.75	2.0	4.0	2.0	0.63	1.2
		5–11	5–11	5–11	5–11	5–11	5–11
5.5	0.160	1.01(6)	−0.28(6)	0.51(5)	0.90(4)	0.75(6)	1.9(2)
		1.3	0.18	0.28	1.3	0.69	0.55
		5–10	4–9	4–9	5–10	6–11	5–10
5.6	0.156*S*	1.00(4)	−0.13(3)	0.54(2)	0.86(2)	0.96(4)	2.7(2)
		3.0	0.66	0.53	0.85	0.59	1.6
		6–12	5–10	5–10	6–12	7–12	7–12
5.6	0.156	1.03(5)	−0.12(3)	0.55(1)	0.86(2)	0.93(4)	2.6(2)
		1.4	0.63	0.56	1.4	2.3	0.50
		5–10	4–8	4–10	4–10	7–12	6–10
5.6	0.157*S*	1.12(8)	−0.17(5)	0.56(2)	0.86(3)	1.07(8)	3.0(5)
			1.9	1.3	0.86	1.5	
			5–9	5–11	5–9	7–12	
5.6	0.157		−0.18(6)	0.58(2)	0.89(3)	1.06(8)	

TABLE XV. Nonsinglet scalar density and axial-vector current matrix elements for quenched lattices at $\beta=6.0$. An estimate of the renormalization constant for the axial-vector current is $Z_A^L/f\sim 0.86$. The notation is as in Table VIII (a).

κ	fF_S/Z_S^L	fD_S/Z_S^L	fF_A/Z_A^L	fD_A/z_A^L	$f\rho_S/Z_S^L$	$f\Delta_S/Z_S^L$
	2.2	1.4	0.56	1.1	0.73	2.0
	6–13	4–10	6–13	6–13	7–11	7–13
0.154*S*	0.99(6)	−0.13(4)	0.55(2)	0.77(3)	1.05(8)	3.4(3)
	1.2	0.59	0.89	0.57	1.6	1.0
	7–12	5–9	7–13	5–11	10–15	10–15
0.154	1.02(6)	−0.11(4)	0.55(2)	0.81(2)	1.12(10)	3.2(5)
	2.9	2.5	0.43	0.69	0.58	0.76
	7–12	4–8	7–12	7–12	7–12	7–12
0.155*S*	1.13(15)	−0.21(8)	0.58(4)	0.83(8)	1.06(12)	3.5(5)
	1.5	0.89	1.5	1.2	1.3	0.56
	8–12	5–9	8–12	8–12	10–14	9–13
0.155	1.22(15)	−0.21(9)	0.56(6)	0.83(8)	1.16(17)	3.1(6)

the extrapolation to the chiral limit of F_A and D_A data may be reliable. Assuming this, we can compare our results to experiment. To be concrete we average the results at $\beta=5.5$ and 5.6, yielding $fF_A/Z_A^L\approx 0.56$ and $fD_A/Z_A^L\approx 0.87$. For our values of κ, the parameter f varies between 0.97 and 0.94. Perturbative and nonperturbative estimates of Z_A^L lie in the range 0.80–0.86 [27]. Taking $Z_A^L/f\approx 0.86$ as a reasonable estimate, we get $F_A\approx 0.48$ and $D_A\approx 0.75$, which are close to the experimental values (Table XIII). This comparison is most reliable for F_A/D_A, where renormalization factors cancel.

We now turn to the scalar matrix elements in the proton, F_S and D_S. First we note that our sources have improved the signal compared to that for the point sources of Ref. [22]. Our results are of comparable quality to those of Ref. [23], which are also obtained using smeared sources. The most notable trend in our results is that $|D_S|$ increases as the quark mass decreases. There is some evidence for a small increase in F_S. These trends have been observed in quenched calculations [22,23], and are required if the results are to extrapolate to the experimental values. Our results with dynamical fermions are in reasonable agreement with quenched results (both those of Refs. [22] and [23] and our own [20]), if we compare them at the same M_π/M_ρ.

In principle, we can extrapolate F_S and D_S to the SU(3)-symmetric point, and use the continuum baryon-octet mass splittings to extract the lattice value for $m_s-(m_u+m_d)/2$ (see the first reference in [23]). This must be divided by the (poorly known) renormalization constant Z_S^L to be compared to the continuum quark masses. The extrapolated value of the ratio D_S/F_S requires no renormalization and can be compared directly to experiment. In practice, however, we do not think our data merits such an extrapolation. We only note that D_S/F_S is rapidly becoming more negative. This indicates the onset of relativistic motion of the bound quarks.

Our results for ρ_S and Δ_S show an increase with β. Such a trend is consistent with renormalizaton-group scaling due to the anomalous dimension of the scalar density. There is no obvious pattern of variation with quark mass. The only constant feature is that $\Delta_S/\rho_S\approx 2.5-3$, which is consistent with quenched results [23]. This result is to be compared with the experimental value of ≈ 3.5 and the infinite quark mass limit of 3.

The most interesting results concern the pion-nucleon σ term, for here we can see clearly the effect of dynamical quarks. Recall that

$$\sigma_{\pi N}=\overline{m}\,\langle N|(\bar{u}u+\bar{d}d)^{\rm cont}|N\rangle\ , \tag{7.4}$$

where $\overline{m}=0.5(m_u+m_d)$. We cannot directly calculate $\sigma_{\pi N}$ as this requires extrapolating the matrix element to very small quark masses. What we can do is calculate the ratio of the full matrix element (valence plus sea) to its valence part, which is given by $\sigma_{\pi N}^{\rm val}\equiv(3F_S-D_S)$. This gives an indication of the importance of insertions on quark loops.

We calculate the full matrix element, including sea contributions, by taking numerical derivatives of the hadron masses

$$\langle N|(\bar{u}u+\bar{d}d)^{\rm cont}|N\rangle=\frac{Z_S^L}{f}\frac{\partial M_N}{\partial(1/2\kappa)}\ . \tag{7.5}$$

Using the numerical derivative circumvents the calculation of the noisy three-point function of Fig. 14(b), but does require a number of data points to get a stable result. Since we take the ratio of this quantity to a similar (valence) matrix element, we need not worry about the factor of Z_S^L/f needed to convert the matrix element to continuum normalization. Our data are shown in Fig. 16, where the valence part is the average of the values at the two κ used in the derivative. We see that the sea contribution is 1–2 times the valence part. This is qualitatively in agreement with our previous results at stronger coupling, and with the experimental data. For more discussion, see Refs. [25] and [28].

We also find a similar factor of 2–3 between the valence and the full value for both ρ_S and Δ_S. Furthermore, the magnitude of the matrix element is roughly

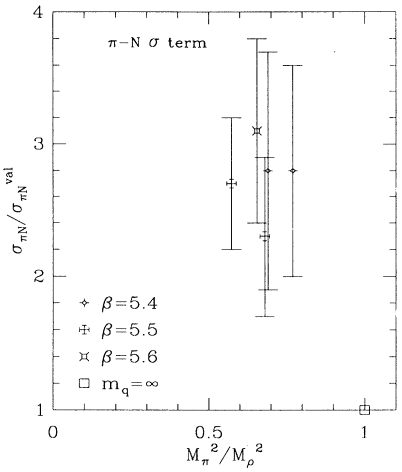

FIG. 16. Ratio of the full σ term to its valence component shown in Fig. 14(a) plotted as a function of $(M_\pi/M_\rho)^2$.

proportional to the number of valence quarks. This is in agreement with a model for constituent quarks in which the quarks are dressed strongly, and in a manner which is independent of the state that they are in.

As a check, we can repeat the analysis with the quenched data. Here the two methods should agree. For example, the average value of $f(3F_S-D_S)/Z_S^L$ for the proton at $\kappa=0.154$ and 0.155 is 3.4(5) from Table XV, while taking the numerical derivative gives 3.5(9) using data in Table XII.

The above calculation do not provide a first-principles result for $m_s\langle P|\bar{s}s|P\rangle$, i.e., the strange-quark contribution to the proton's mass. For this we need $\partial M_P/\partial m_s$, evaluated holding the masses of u,d quarks at their physical values and varying the strange-quark mass near $m_s\approx 25\bar{m}$. Such a calculation is still a number of years away.

VIII. CONCLUSIONS

We use the HMC algorithm to simulate QCD with two flavors of Wilson fermions on 16^4 lattices down to the strange-quark mass. The CM2 is very well suited to run QCD in production mode and the present version of the code for updating $16^3\times 32$ lattices runs at a sustained speed of 1.3 Gflops on a 16K machine.

The preconditioned over-relaxed algorithm we proposed for matrix inversion is very efficient: the convergence is exponential for all values of the parameters we have used so far. The step size used in molecular-dynamics evaluation has to be decreased as $m_q^{3/4}$ as shown by Gupta *et al.* [8]. While this is a much weaker dependence on the quark mass for HMC algorithm than the worst-case scenario proposed by us, the CPU time still scales as $m_\pi^{-10.5}$. Thus a major improvement in algorithms is still necessary in order to probe the chiral limit of QCD.

Our runs are not long enough to measure autocorrelation times, but we suspect that decorrelation times are of order a few hundred trajectories. This translates to approximately 1000 Gflop hours to produce a decorrelated $16^3\times 32$ lattice at $m_q\sim m_s$.

We have presented detailed results for Wilson loop expectation values for a number of values of β and κ. From this data we extract the potential between a heavy $\bar{q}q$ pair for $r\leq 0.5$ fm. This separation is too short to demonstrate screening due to vacuum polarization. However, the results are qualitatively different from those obtained in the pure gauge theory.

We calculate quark propagators using the Wuppertal smearing method. We find a strong signal in the hadron correlators and find that the lowest state starts to dominate for t in the range 6–9. This allows us to extract accurate mass estimates for pions on our lattices. The signal for the rho and the nucleon is not as good and systematic and statistical errors could be as big as 5%. We have made a detailed comparison with quenched results and find qualitatively similar behavior for the two theories. This, we feel, is not unexpected for $m_q\geq m_s$.

We show that a good signal is obtained in three-point correlation functions of the nonsinglet scalar density and axial-vector current operators inside hadrons. The reduced matrix elements F_A and D_A show little variation with β or the quark mass and their values are consistent with experimental numbers even though $m_q\geq m_s$.

In case of the matrix elements of the scalar density, we find that the contribution from insertions on the sea quarks is comparable to the valence contribution. Since the valence contribution to the pion-nucleon σ term is ≈ 26 MeV, our result suggests a value closer to the experimental number of 45–65 MeV for the full theory [29].

ACKNOWLEDGMENTS

The 12^4 lattices were generated at the Pittsburgh Supercomputing Center. We are very grateful to R. Roskies for the allocation of time on the YMP. The 16^4 lattices were updated on the Connection Machines at Los Alamos National Laboratory, Sandia National Laboratory, NPAC at Syracuse, Thinking Machines and Argonne National Laboratory. We thank Carl Diegert, Geoffrey Fox, Paul Messina, John Mucci, and Andy White for the tremendous support shown to us over the last two years. The propagator calculation was done on Cray YMP at LANL during their shakedown period. We thank Charlie Slocomb, Norm Morse, and Andy White for their support. For the quenched calculations we acknowledge the tremendous support provided by NERSC at Livermore, Pittsburgh Supercomputing Center, and San Diego Supercomputer Center. The research of C.F.B. was partly supported by DOE Grants Nos. DE-FG03-85eR25009 and DE-AC03-81ER40050, by AFOSR Grant No. AFOSR-89-0422. S.R.S. was supported in part by the DOE Outstanding Junior Investigator office through Contract No. DE-AT06-88ER40423 and the Alfred P. Sloan Foundation. This research was supported in part by the National Science Foundation under Grant No. PHY89-04035.

APPENDIX A: PERFORMANCE OF THE HMC ALGORITHM ON CM2

Our QCD code is written in *LISP with computationally intensive matrix multiplications written in CMIS (Connection Machine Instruction Set). It runs at a sustained speed of 1.6 Gflops on a 32-bit machine. The code performance has been further enhanced to 5.3 Gflops on the latest versions of the CM2 with 64-bit Weitek coprocessors and 256 kbyte of memory per processor. Both performance numbers have been prorated to the full 64K processor machine. For comparison the same problem sustains ≈ 1 Gflop on an 8 processor Cray YMP.

The larger memory CM2 allows us to rearrange the data to make memory access more efficient, though the major part of the speed up comes from using multiwire news instructions (facility provide by the Thinking Machines Corporation to do simultaneous bidirectional communications in four dimensions). With this performance we can carry out detailed calculations with two flavors of Wilson fermions on $16^3 \times 32$ lattices on the CM2. The details of the implementation have been presented in Ref. [30].

The issue of machine precision is very important for the stability of the HMC algorithm. The present calculations on the CM2 have all been done using the 32-bit Weitek chips. We find that 32-bit precision is adequate for the gauge part of the calculation. In the remaining part of the code, loss of precision with 32-bit arithmetic can arise in three ways, but as explained below none of these presented a problem on the CM2.

(1) Roundoff errors at each step of the inversion of the fermion operator: for QCD the number of arithmetic operations necessary per site is approximately 1500. This number is independent of the lattice volume, since the Dirac operator involves only nearest-neighbor sites. There are no divisions in the arithmetic operations, and all numbers are of order unity. For such a computation 32-bit precision is adequate. In iterative algorithms (e.g., conjugate gradient, minimal residue etc.), one also performs a global sum over sites. These inner products involve the residue vector, the elements of which are small and fluctuate in sign, so the accumulant stays small. To make sure that roundoff errors do not build up in the residue vector we use the following test: we run a trajectory of 100 MD steps, (each step takes on average 150 iterations for matrix inversion, i.e., 600 matrix multiplications, at $m_q \approx m_s$), two different ways: (a) the residue is calculated only at the beginning of each inversion, and (b) the residue vector is recalculated every 10 iterations. We find that the difference after 100 MD steps is typically in the ninth significant figure for each of the three terms in the action; this is a negligible error for the present set of parameters. In production runs we recalculate the residue every 20 iterations as an additional precaution, since the overhead is small.

(2) Global sums: For a 16^4 lattice one adds $\approx 1.6 \times 10^6$ numbers in a global accumulate. Even for sums involving numbers of the same sign and approximately of unit magnitude we do not need any special algorithms to circumvent adding small numbers to a large accumulant, since on the CM2 all intrinsic global accumulate functions use a binary tree involving nearby sites. Thus at each step numbers of comparable magnitude are added. Also, in each iteration the result of global sum multiplies the over-relaxation parameter. Since the performance of the algorithm is insensitive to the precise value of this parameter ω (as long as it is in the range 1.15–1.5 [2]), errors due to lack of precision in the global sum are equivalent to small fluctuations in ω for that iteration. Lastly, our implementation of the minimal residue algorithm is self-correcting: if a systematic drift does exist due to 32-bit arithmetic, it is removed by the periodic recalculation of the residue vector as explained above.

(3) Accumulating ΔS: The three terms in the action (pseudofermion, momentum, and gauge field) are all of order 10^6 on a 16^4 lattice. For $\approx 70\%$ acceptance in the Metropolis step ΔS has to be of order 1. It is clear that for this step the 32-bit accuracy is not sufficient if one wishes to monitor the three terms separately. We, therefore, convert the value for each of three terms at each site to 64 bits before doing the global sum and then evaluate ΔS in 64-bit precision. The performance of the code is not affected by this step, since this global sum over the lattice has to be done only once per trajectory. Alternatively, one can first calculate ΔS at each site. Since this result is small and fluctuates in sign from site to site, the final global accumulate can be done in 32-bit precision.

The latest versions of the Connection Machine use 64-bit Weitek chips. The advantage of using 32-bit data is much better performance due to more efficient use of registers and from half as much memory access. Our conclusion based on the above analysis is that the HMC algorithm runs efficiently and without precision problems with either 32-bit or 64-bit data structures for $m_q \geq m_s$.

APPENDIX B: CALCULATING MATRIX ELEMENTS

In this appendix we explain how the result Eq. (7.1) is derived, emphasizing the approximations that are made. Nearly all of the following discussion is drawn from Refs. [22], [23], and [9]. Our aim is to collect the arguments in one place, and to clarify certain subtleties.

We wish to calculate the matrix elements of bilinear operators between hadron states (denoted generically by $|p\rangle$):

$$\mathcal{M}_\Gamma = \langle p | \mathcal{O}_\Gamma | p \rangle \ , \quad \mathcal{O}_\Gamma = \int_{\mathbf{x}} \bar{q}(\mathbf{x}) \Gamma q(\mathbf{x}) \ . \tag{B1}$$

In the following discussion we are not concerned with spin factors, and so proceed as though the hadron is spinless. We use the normalization $\langle p | p \rangle = 1$, which is the standard normalization for baryons at rest, though it is nonstandard for mesons.

To calculate these matrix elements in continuum QCD, we can use Euclidean two- and three-point correlators. The two-point function behaves at large t as

$$\langle \mathcal{P}(t) \mathcal{P}(0) \rangle = \int d\mu \, \mathcal{P}(t) \mathcal{P}(0) e^{-S} \underset{t \to \infty}{\sim} z e^{-M_p t} \ , \tag{B2}$$

where $\mathcal{P}$ is an interpolating field with $\mathbf{p} = 0$, and $d\mu$ is the usual measure in the functional integral. M_p is the mass

of lightest hadron with the same quantum numbers as $\mathcal{P}$. The three-point function, with an operator inserted at time τ, behaves for large τ and $t-\tau$ as

$$\left\langle \mathcal{P}(t)\int_{\mathbf{x}}[\bar{q}(\mathbf{x},\tau)\Gamma q(\mathbf{x},\tau)]\mathcal{P}(0)\right\rangle_{\text{conn}} \underset{\substack{t-\tau\to\infty\\ \tau\to\infty}}{\sim} Ze^{-M_p(t-\tau)}\mathcal{M}_\Gamma e^{-M_p\tau} . \quad \text{(B3)}$$

Thus we can extract $\mathcal{M}_\Gamma$ from the ratio

$$R_\Gamma(\tau)=\frac{\left\langle \mathcal{P}(t)\int_{\mathbf{x}}[\bar{q}(\mathbf{x},\tau)\Gamma q(\mathbf{x},\tau)]\mathcal{P}(0)\right\rangle_{\text{conn}}}{\langle \mathcal{P}(t)\mathcal{P}(0)\rangle} \underset{\substack{t-\tau\to\infty\\ \tau\to\infty}}{\sim} \mathcal{M}_\Gamma . \quad \text{(B4)}$$

In lattice QCD we evaluate essentially the same quantities, except that integrals are replaced by sums, and the correlators are defined only for discrete values of t. Since the lattice correlators go over to those of the continuum when the lattice spacing vanishes, we use the lattice version of Eq. (B4) to define the lattice matrix element

$$\mathcal{R}_\Gamma^L(\tau)=\frac{\left\langle \mathcal{P}(t)\sum_{\mathbf{x}}[\bar{q}(\mathbf{x},\tau)\Gamma q(\mathbf{x},\tau)]\mathcal{P}(0)\right\rangle}{\langle \mathcal{P}(t)\mathcal{P}(0)\rangle} \underset{\substack{t-\tau\to\infty\\ \tau\to\infty}}{\sim} \mathcal{M}_\Gamma^L . \quad \text{(B5)}$$

$\mathcal{M}_\Gamma^L$ differs from $\mathcal{M}_\Gamma$ by terms of $O(g^2)$ and of $O(a)$. In our actual calculations we extract $\mathcal{M}_\Gamma^L$ using

$$\mathcal{R}_\Gamma^L\equiv\sum_\tau \mathcal{R}_\Gamma^L(\tau) \underset{t\to\infty}{\sim} \text{const}+t\mathcal{M}_\Gamma^L . \quad \text{(B6)}$$

To derive this equation we note that, by summing over all τ, we are combining three contributions: (a) the "on-shell" matrix element of Eq. (B3) ($t>\tau>0$); (b) that from excited states ($\tau\sim 0$ and $\tau\sim t$); and (c) that from "off-shell" terms ($\tau>t$ and $\tau<0$). The "on-shell" term depends linearly on t, because each extra time slice gives an identical contribution of the form of Eq. (B3). The other contributions, however, are independent of t aside from exponential tails.

Numerical calculations are done at finite lattice spacing. To quote results in physical units, one needs to know the relationship between the lattice matrix element $\mathcal{M}_\Gamma^L$ and the desired continuum matrix element $\mathcal{M}_\Gamma$. There are two parts to this relation. First, the lattice operators have to be converted to continuum normalization. This necessitates the calculation of the Z factors, which account for all terms which are functions of g^2, both perturbative and nonperturbative:

$$[\bar{q}(x)\Gamma q(x)]^{\text{cont}}=Z_\Gamma^L[\bar{q}(x)\Gamma q(x)]^L+O(a) . \quad \text{(B7)}$$

The Z factors approach unity only as $O(g^2)=O(1/\ln(a))$ in the continuum limit, and are thus more important than the $O(a)$ corrections from small enough a. Ideally they should be calculated nonperturbatively, but in many cases only perturbative results are available. They have been extensively discussed in the literature (see Ref. [22], and references therein). We have, wherever possible, presented results as ratios of matrix elements in order to cancel such factors. For mass splittings, Z_S^L cancels in the renormalization-group-invariant combination $m_q\bar{q}q$.

Second, we consider the $O(a)$ terms in the relation between $\mathcal{M}_\Gamma^L$ and $\mathcal{M}_\Gamma$. To remove these terms one has to "improve" not only the operators [31] but also the action [32]. This means that, for a given operator, the $O(a)$ terms depend on the initial and final states, and thus cannot be removed by a multiplicative factor. On dimensional grounds there are two types of $O(a)$ terms one has to consider: $O(\Lambda_{\text{QCD}}a)$ and $O(m_q a)$ ignoring g^2 dependence. Even though we cannot tackle $O(\Lambda_{\text{QCD}}a)$ corrections in our present set up, we can account for certain known $O(m_q a)$ terms by defining

$$\mathcal{M}_\Gamma^L=f_\Gamma(m_q a)\mathcal{M}_\Gamma/Z_\Gamma^L+O(a) . \quad \text{(B8)}$$

In particular, one can calculate the ratio in Eq. (B5) for very heavy quarks (i.e, $\kappa\to 0$) using a hopping-parameter expansion. The results are correct except for an overall factor 2κ. By "correct" we mean that the scalar matrix elements count the number of quarks, the axial-vector matrix elements measure the quark spins, etc. So f_Γ should have the limiting behavior

$$f_\Gamma=\begin{cases}1 & \text{for } \kappa\to\kappa_c ,\\ 2\kappa & \text{for } \kappa\to 0 ,\end{cases} \quad \text{(B9)}$$

for each Γ.

To choose a form for f_Γ which interpolates between these limits, it is helpful to use an alternative expression for $\mathcal{M}_\Gamma^L$. If we add a source term to the action, $\delta S_\Gamma=h_\Gamma\sum_x\bar{q}(x)\Gamma q(x)$, then we have that

$$\mathcal{R}_\Gamma^L=-\frac{\partial}{\partial h_\Gamma}\ln\langle \mathcal{P}(t)\mathcal{P}(0)\rangle\Big|_{h_\Gamma=0} . \quad \text{(B10)}$$

Equation (B2) still applies for the two-point function, except that M_p now depends on h_Γ. Thus for large t,

$$\mathcal{R}_\Gamma^L=\text{const}+t\frac{\partial M_p}{\partial h_\Gamma}\Big|_{h_\Gamma=0} , \quad \text{(B11)}$$

so, comparing with Eq. (B6), we find that

$$\mathcal{M}_\Gamma^L=\frac{\partial M_p}{\partial h_\Gamma}\Big|_{h_\Gamma=0} . \quad \text{(B12)}$$

Now, for the scalar matrix element the source h_S just adds to the mass term in the Lagrangian, which is

$$m_q^{\text{Lag}}=\frac{1}{2}\left[\frac{1}{\kappa}-\frac{1}{\kappa_c}\right] . \quad \text{(B13)}$$

Thus we can rewrite Eq. (B12) as

$$\mathcal{M}_S^L=\frac{\partial M_p}{\partial m_q^{\text{Lag}}} . \quad \text{(B14)}$$

At finite lattice spacing, it is more appropriate to use Wilson's definition of quark mass (which is based on the expression for the pole mass in free field theory):

$$m_q = \ln\left[1+\frac{1}{2}\left[\frac{1}{\kappa}-\frac{1}{\kappa_c}\right]\right] . \tag{B15}$$

Such a modification ensures, for example, that the proton mass is three times the quark mass for heavy quarks. Thus we define f_S such that

$$\frac{\mathcal{M}_S^L}{z_S^L} = \frac{\partial M_p}{\partial m_q} , \tag{B16}$$

which requires

$$f_S = \frac{\partial m_q}{\partial m_q^{\text{Lag}}} = \frac{1}{1+\frac{1}{2}\left[\frac{1}{\kappa}-\frac{1}{\kappa_c}\right]} . \tag{B17}$$

This choice satisfies both criteria of Eq. (B9). For simplicity, we adopt this choice for all f_Γ. We emphasize, however, that this choice is not unique, nor do we claim that it takes care of all $O(a)$ corrections.

[1] S. Duane, A. Kennedy, B. Pendleton, and D. Roweth, Phys. Lett. B **195**, 216 (1987).
[2] R. Gupta, A. Patel, C. Baillie, G. Guralnik, G. Kilcup, and S. Sharpe, Phys. Rev. D **40**, 2072 (1989).
[3] R. Gupta, in *Lattice '90,* Proceedings of the Conference, Tallahassee, Florida, 1990, edited by U. M. Heller, A. D. Kennedy, and S. Sanielevici [Nucl. Phys. B (Proc. Suppl.) **20**, 385 (1991)].
[4] D. Daniel, R. Gupta, and D. Richards, Phys. Rev. D **43**, 3715 (1991).
[5] P. Mackenzie, Phys. Lett. B **226**, 369 (1989).
[6] A. Patel, in *Lattice '89,* Proceedings of the International Symposium, Capri, Italy, 1989, edited by R. Petronzio *et al.* [Nucl. Phys. B (Proc. Suppl.) **17**, 509 (1990)].
[7] R. Gupta, G. Kilcup, and S. Sharpe, Phys. Rev. D **38**, 1278 (1988); in *Lattice '88,* Proceedings of the International Symposium, Batavia, Illinois, 1988, edited by A. S. Kronfeld and P. B. Mackenzie [Nucl. Phys. B (Proc. Suppl.) **9**, 473 (1989)].
[8] S. Gupta, A. Irbäck, F. Karsch, and B. Petersson, Phys. Lett. B **242**, 437 (1990).
[9] S. Güsken, U. Löw, K. -H. Mütter, R. Sommer, A. Patel, and K. Schilling, Phys. Lett. B **227**, 266 (1989).
[10] S. Güsken, in *Lattice '89* [6], p. 361.
[11] T. DeGrand and R. Loft, Report No. COLO-HEP-223 (unpublished).
[12] D. Toussaint, in *Lattice '90* [3], p. 362.
[13] R. Gupta, G. Guralnik, G. Kilcup, and S. Sharpe, Phys. Rev. D **43**, 2003 (1991).
[14] P. Geiger and N. Isgur, Phys. Rev. D **41**, 1595 (1990).
[15] APE Collaboration, P. Bacilieri *et al.*, Phys. Lett. B **214**, 115 (1988); APE Collaboration, S. Cabasino *et al.*, *ibid.* **258**, 195 (1991).
[16] S. Ono, Phys. Rev. D **17**, 888 (1978).
[17] R. Gupta, in *Lattice '89* [6], p. 70.
[18] R. Gupta, G. Guralnik, G. Kilcup, A. Patel, S. Sharpe, and T. Warnock, Phys. Rev. D **36**, 2813 (1987).
[19] T. DeGrand, in *Lattice '90* [3], p. 353.
[20] D. Daniel, R. Gupta, G. Kilcup, A. Patel, and S. Sharpe (in preparation).
[21] M. Fukugita and A. Ukawa, Phys. Lett. B **203**, 145 (1988).
[22] L. Maiani, G. Martinelli, M. Paciello, and B. Taglienti, Nucl. Phys. **B293**, 420 (1987).
[23] S. Güsken, K. Schilling, R. Sommer, K. -H. Mütter, and A. Patel, Phys. Lett. B **212**, 216 (1988); S. Güsken, K. -H. Mütter, R. Sommer, A. Patel, and K. Schilling, Nucl. Phys. **B327**, 763 (1989).
[24] K. F. Liu, in *Lattice '90* [3], p. 467.
[25] A. Patel, R. Gupta, G. Kilcup, and S. Sharpe, Phys. Lett. B **225**, 398 (1989).
[26] R. Jaffe and A. Manohar, Nucl. Phys. **B337**, 509 (1990).
[27] L. Maiani and G. Martinelli, Phys. Lett. B **178**, 265 (1986).
[28] A. Patel, Phys. Lett. B **236**, 102 (1990).
[29] J. Gasser, H. Leutwyler, and M. E. Sainio, Phys. Lett. B **253**, 252 (1991).
[30] R. Brickner, in *Lattice '90* [3], p. 145.
[31] G. Heatlie, G. Martinelli, C. Pittori, G. Rossi, and C. Sachrajda, Nucl. Phys. **B352**, 266 (1991).
[32] B. Sheikholeslami and R. Wohlert, Nucl. Phys. **B259**, 572 (1985).